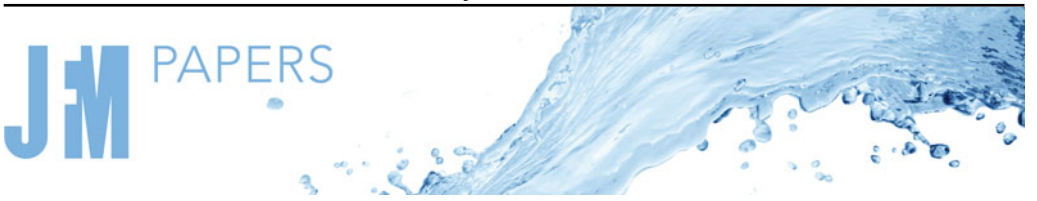
J. Fluid Mech. (2026), *vol.* 1041, A16, doi:10.1017/jfm.2026.11892



A modal Rayleigh method for thermoacoustic analysis of hydrogen–air flames

Borja Pedro-Beltran[1], **Zin Shahin**[1], **Sohel Herff**[2], **Matthias Meinke**[1,3], **Dominik Krug**[1] and **Wolfgang Schröder**[1,3]

[1]Institute of Aerodynamics and Chair of Fluid Dynamics, RWTH Aachen University, Wüllnerstraße 5a, Aachen, Germany

[2]Jülich Supercomputing Centre, Forschungszentrum Jülich GmbH, Wilhelm-Johnen-Straße, Jülich, Germany

[3]JARA Centre for Simulation and Data Science, RWTH Aachen University, Weg 23, Aachen, Germany

Corresponding author: Borja Pedro-Beltran, b.pedro@aia.rwth-aachen.de

(Received 12 November 2025 UTC; revised 8 June 2026 UTC; accepted 28 June 2026 UTC)

A frequency-resolved modal Rayleigh method, in which the classical Rayleigh criterion is reformulated using dynamic mode decomposition (DMD), is presented. This approach yields mode-specific, closed-form measures of thermoacoustic excitation and absorption. The framework reconstructs pressure and heat-release fields with an acoustic scaling, separates self- and cross-modal contributions through a finite-time kernel and augments the in-phase Rayleigh term with a phase-invariant quadrature efficiency to quantify the coupling magnitude. The method is applied to two-dimensional, acoustically forced, anechoic hydrogen–air slit flames at four equivalence ratios ($\phi = 0.4$, 0.5, 0.6, 0.7) excited at 220, 437 and 800 Hz, in addition to multi-tone forcing. The analysis shows that the flame–acoustic coupling is primarily concentrated near the flame tip, that the coupling strength and frequency response vary systematically with equivalence ratio and that low-frequency forcing promotes nonlinear energy transfer into higher harmonics. Lean flames remain near linear and decouple at high frequency, whereas richer flames that lock in at higher-frequency excitation exhibit stronger nonlinear distortion at lower frequencies. Where the modal Rayleigh index is positive, the far-field sound pressure level increases at the corresponding frequency, confirming that the proposed metrics isolate feedback-effective modes. Overall, the DMD-based modal Rayleigh method provides a compact, mode-resolved description of flame–acoustic interactions.

Key words: acoustics, combustion, laminar reacting flows

© The Author(s), 2026. Published by Cambridge University Press.

https://doi.org/10.1017/jfm.2026.11892 Published online by Cambridge University Press

1. Introduction

Hydrogen is increasingly regarded as a key enabler of a decarbonised energy future due to its ability to store renewable energy through electrolysis and subsequently release it via combustion in gas turbines to ensure grid stability (Beer 2000). Its versatility extends beyond stationary power generation to aviation. The replacement of kerosene by hydrogen could enable cleaner long-distance flights (Yusaf *et al.* 2024). Within gas turbines and aircraft engines, however, combustion instabilities remain a critical challenge (Noble *et al.* 2021). These instabilities arise from the complex interaction between chemical reactions, fluid dynamics and acoustics, and represent one of the most difficult phenomena in combustion science (Poinsot 2017). Effective prediction and control are therefore essential for practical implementation. The mechanisms driving combustion instability are inherently complex and may be induced by multiple factors (Lee & Santavicca 2003). They are particularly pronounced in lean-premixed combustion, which has become the preferred approach over non-premixed combustion due to its ability to reduce NOx emissions and meet stringent environmental regulations (Lefebvre & Ballal 2010; Ferrarotti *et al.* 2021). In such systems, the interaction between the flame and acoustics plays a dominant role in the onset of instability (Lieuwen 2003). Thermoacoustic instabilities arise when the unsteady heat release from a flame couples constructively with the acoustic pressure oscillations within the combustor geometry, such that the acoustic input of energy exceeds its dissipation rate (Candel 2002; Poinsot 2017; Lieuwen 2021).

An important consideration in developing gas turbine combustors capable of operating with pure hydrogen or hydrogen-enriched natural gas is therefore the substantial modification in thermoacoustic instability characteristics introduced by these fuels (Aguilar *et al.* 2022). The unique properties of hydrogen, such as high diffusivity, wide flammability limits and elevated laminar flame speeds, produce flame–acoustic interactions that differ significantly from those of hydrocarbon-based systems. Furthermore, hydrogen flames exhibit preferential diffusion and non-equidiffusion effects within the preheat zone, which influence their dynamic response to perturbations (Bechtold & Matalon 2001; Boushaki *et al.* 2012; Beerer *et al.* 2014).

Recent studies have investigated the effect of hydrogen enrichment on the flame dynamics and thermoacoustic responses in laminar and turbulent hydrogen–methane burners (Æsøy *et al.* 2020; Lim *et al.* 2021; Garcia *et al.* 2024). Increasing hydrogen concentration has been shown to shorten the flame, making it more compact and stabilising it closer to the flame holder (Aguilar *et al.* 2022). Such compact flames respond to acoustic velocity fluctuations across a broader range of frequencies, a behaviour typically quantified using the flame transfer function (FTF), which relates heat-release rate (HRR) fluctuations to imposed acoustic velocity perturbations (Schuller *et al.* 2020). For nonlinear responses, a flame describing function, or nonlinear FTF, is often employed (Noiray *et al.* 2008). Studies have reported that increasingly compact premixed flames exhibit higher gain cutoff frequencies and reduced time delays, making hydrogen-enriched flames more susceptible to thermoacoustic instabilities (Lim *et al.* 2021). These higher cutoff frequencies also enhance sensitivity to convective disturbances, presenting both challenges and opportunities for active instability control (Park *et al.* 2022).

Laminar premixed conical and slit flames are widely used as canonical configurations to develop a fundamental understanding of the flame dynamics. The linear and nonlinear responses of such flames to forced excitation have been analysed in several numerical works (Albayrak *et al.* 2014; Karimi 2014; Schlimpert *et al.* 2016; Lim *et al.* 2021; Yang *et al.* 2021; Vance *et al.* 2023*a*; Rodríguez-Pastor *et al.* 2024; Zheng *et al.* 2024), as well as characterised in high-fidelity experimental flame imaging campaigns. However, most

https://doi.org/10.1017/jfm.2026.11892 Published online by Cambridge University Press

of these studies have focused on methane flames and relied on the level-set method and G-equation analysis.

Notably, experimental works on mesoscale multi-nozzle and multi-slit arrays (Lee & Kim 2020; Kang & Kim 2021; Park *et al.* 2022; Kang *et al.* 2023) have shown, using phase-resolved OH^* chemiluminescence and OH-Planar Laser Induced Fluorescence, that compact lean-premixed hydrogen flames preferentially couple to high-frequency eigenmodes and that the collective dynamics of the flame ensemble governs the onset of self-excited instabilities. The influence of flow unsteadiness on the local and global dynamics of acoustically excited laminar premixed hydrogen–air flames was addressed in Zhang *et al.* (2022), where it was shown that the fluctuation time scale plays a significant role in the flame–flow interaction. More recently, Vance *et al.* (2023*b*) studied the stabilisation mechanism of an H_2–air slit flame in a narrow channel, and Dupuy *et al.* (2024) investigated the control of intrinsic thermoacoustic instabilities in a similar configuration. Nevertheless, detailed analyses of acoustically excited H_2–air flames remain relatively scarce.

The most widely used criterion to assess the stability of thermoacoustic systems, such as gas turbine combustors or rocket motors, is the physical feedback mechanism proposed by Lord Rayleigh (1878), which was formalised into a mathematical index form by Putnam (1971). This criterion states that acoustic energy increases when the unsteady heat-release rate is sufficiently in phase with acoustic pressure that the work done by gas expansion exceeds the dissipated energy over a cycle. While effective, the Rayleigh criterion does not account for the effect of a mean flow (Magri *et al.* 2020). More general formulations have therefore been developed to incorporate mean-flow effects (Nicoud & Poinsot 2005; George & Sujith 2011, 2012).

Data-driven decomposition techniques such as dynamic mode decomposition (DMD) have emerged as powerful tools to analyse the flame dynamics (Duwig & Iudiciani 2010; Ma *et al.* 2020; Yang *et al.* 2021; Rodríguez-Pastor *et al.* 2024). The idea of representing a spatially resolved Rayleigh criterion was explored by Kopp-Vaughan & Renfro (2012), who applied proper-orthogonal decomposition (POD) to chemiluminescence images and showed that one of the extracted modes correlated strongly with a pseudo-Rayleigh index averaged over time. This demonstrated that fluctuations in flame-front ripples are closely tied to Rayleigh-type feedback between heat release and acoustic pressure. While such studies established the value of combining modal analysis with Rayleigh-type measures, their scope was limited to POD, which identifies energetic spatial structures, but lacks the direct temporal dynamics. Ghani *et al.* (2015) applied DMD to Large Eddy Simulation of a bluff-body stabilised combustor and successfully extracted the structure of self-excited longitudinal and transverse instability modes, but did not connect these modes to a Rayleigh-based stability analysis. Huang *et al.* (2016) applied POD and DMD to a longitudinal rocket combustor and showed that, while POD provides compact representations of energetic structures, DMD is better suited to identify frequency-resolved coupling between pressure and heat release. However, in that framework the Rayleigh criterion was still evaluated in its classical form. That is, it was applied to reconstructed fields rather than to the modes themselves.

The present study advances this approach by formally deriving a modal Rayleigh index (RI) directly from DMD modes. This formalism yields a frequency-resolved, mode-specific measure of thermoacoustic excitation and absorption. It links the classical Rayleigh criterion to the temporal and spatial dynamics of individual modes. Embedding the Rayleigh criterion within the DMD framework enables thermoacoustic excitation to be associated directly with modes of characteristic frequency and growth rate. Hence, it can be determined which oscillatory dynamics is most responsible for satisfying or violating

https://doi.org/10.1017/jfm.2026.11892 Published online by Cambridge University Press

the criterion. To the authors' knowledge, this is the first work to formulate and apply a Rayleigh criterion explicitly at the level of DMD modes. It extends decomposition-based approaches into a fully modal thermoacoustic stability analysis framework.

The unique advantages of the proposed method are threefold: (i) it provides mode-resolved causality by linking thermoacoustic feedback directly to specific frequencies and growth rates; (ii) it isolates the phase-invariant coupling strength from the absolute phase alignment; and (iii) it enables precise spatial and spectral localisation of energy transfer, even in complex, multi-frequency environments.

The remainder of this paper is structured as follows. Section 2 details the derivation of the modal RI, including DMD-based reconstruction with acoustic scaling, decomposition into modal and cross-modal contributions and the quadrature pressure–heat-release correlation. Section 3 describes the numerical framework and the simulation set-up. Section 4 presents results from twelve simulations of hydrogen–air flames. To be more precise, simulations at four equivalence ratios each subjected to three single-frequency forcings are performed. Furthermore, four cases with combined multi-frequency excitation are considered. The thermodiffusively unstable H_2–air flames are deliberately selected as the test configuration since they present a rich spectral environment – externally forced modes across three frequencies, intrinsic thermodiffusive (TD) instability modes and their nonlinear interactions – in which the modal RI directly reveals which frequencies actively drive thermoacoustic excitation, where along the flame this coupling is spatially concentrated and how the dominant coupling frequency shifts with mixture composition. Finally, § 5 summarises the findings and discusses the implications of modal Rayleigh analysis to better understand flame–acoustic interactions in hydrogen combustion systems.

2. Modal RI

The RI is a fundamental measure of thermoacoustic stability since it quantifies the net energy exchange between unsteady heat release and acoustic pressure fluctuations. While its classical definition is expressed in terms of instantaneous fluctuations in physical space and time, this formulation does not directly align with modern modal decomposition techniques.

Dynamic mode decomposition, for instance, represents the flow field in terms of coherent modes with well-defined frequencies and growth rates (Schmid 2010). To interpret these modes in the context of thermoacoustic stability, it is necessary to reformulate the RI in modal terms. Such a derivation provides a direct correspondence between the classical stability criterion and the spectral information obtained from DMD, thereby enabling the identification of pressure modes whose amplitudes are enhanced or reduced by heat-release fluctuations.

The following derivation rigorously establishes this connection. By expressing the RI in terms of modal amplitudes and their interactions, the analysis yields a modal RI that not only retains the physical meaning of the classical formulation, but also facilitates the systematic evaluation of thermoacoustic energy transfer within a modal decomposition framework.

The classical RI, as mathematically formalised by Putnam (1971), is defined for a spatial location $\boldsymbol{x}$ over a time window T as

$$\mathcal{R}(\boldsymbol{x}; T) = \frac{1}{T}\int_{t_0}^{t_0+T} p'(\boldsymbol{x}, t)\, \dot{q}'(\boldsymbol{x}, t)\, \mathrm{d}t, \tag{2.1}$$

where p' denotes the acoustic pressure fluctuation and $\dot{q}'$ the fluctuating volumetric heat-release rate. A positive RI implies that, averaged over T, the heat-release rate is

https://doi.org/10.1017/jfm.2026.11892 Published online by Cambridge University Press

in phase with the pressure, thus driving the acoustic field. A negative value indicates that the heat-release rate fluctuations are, on average, negatively correlated with the acoustic pressure (in antiphase, i.e. opposing it rather than in quadrature), so that the heat-release source term does negative work on the acoustic field and extracts energy from it rather than supplying it. We refer to this as local acoustic absorption, meaning a negative contribution to the heat-release source term in the acoustic energy balance at that location or mode. It should be distinguished from system-level damping, i.e. acoustic propagation losses, viscous dissipation, acoustic-to-vortical energy transfer, etc., which represents true dissipation of acoustic energy and is beyond the scope of the Rayleigh criterion (Schuermans *et al.* 2023). Whether a thermoacoustic system is unstable therefore depends on whether the net driving from heat release exceeds the total dissipation, which must be assessed separately.

To facilitate a modal analysis, complex analytic signals $P(\boldsymbol{x}, t)$ and $Q(\boldsymbol{x}, t)$ which correspond to p' and $\dot{q}'$ are introduced. They contain only positive frequencies. The real-valued fluctuations are obtained via

$$p'(\boldsymbol{x}, t) = \frac{1}{2}\left[P(\boldsymbol{x}, t) + P^*(\boldsymbol{x}, t)\right], \quad \dot{q}'(\boldsymbol{x}, t) = \frac{1}{2}\left[Q(\boldsymbol{x}, t) + Q^*(\boldsymbol{x}, t)\right]. \tag{2.2}$$

The product in (2.1)

$$p'\,\dot{q}' = \frac{1}{4}\left[PQ + PQ^* + P^*Q + P^*Q^*\right] \tag{2.3}$$

has four contributions PQ, P^*Q^*, PQ^* and P^*Q. The terms PQ and P^*Q^* oscillate at the sum of the pressure frequency ω_p and heat-release rate frequency ω_q. In the limit of an infinitely long averaging window $T \to \infty$, their time averages vanish identically

$$\lim_{T\to\infty} \frac{1}{T} \int_{t_0}^{t_0+T} \left(PQ + P^*Q^*\right) \mathrm{d}t = 0. \tag{2.4}$$

For finite T, these terms do not cancel exactly, but their contribution is weighted by the window transfer function $W(\omega_p + \omega_q)$. For a rectangular window $W(\Omega) = \mathrm{sinc}(\Omega T/2)$, defined as $\mathrm{sinc}(x) = \sin(\pi x)/(\pi x)$. Since $\omega_p + \omega_q$ is typically large, $|W(\omega_p + \omega_q)|$ is small and the residual sum-frequency contribution is negligible in practice.

The remaining terms PQ^* and P^*Q oscillate at the difference frequency $\omega_p - \omega_q$. They capture the physically relevant in-phase interaction between p' and $\dot{q}'$. When the two contributing components have the same frequency, called a self-interaction, the difference frequency vanishes and the associated Rayleigh contribution remains finite. When they have different frequencies, called a cross-interaction, the difference frequency may be small, in which case $|W(\omega_p - \omega_q)|$ decays slowly and a residual off-diagonal contribution can survive. This effect is commonly termed cross-modal leakage.

An important special case occurs when all modal frequencies lie on a perfect harmonic grid, $\omega = n\,\omega_{min}$, and the averaging window is an integer multiple of the fundamental period, $T = m\,(2\pi/\omega_{min})$. Then, the sum-frequency terms cancel each other for each pair, and the difference-frequency terms vanish unless the two components have the same frequency. Thus, cross-modal leakage does not occur under grid-aligned averaging.

Neglecting the sum-frequency terms and retaining only the difference-frequency interaction yields

$$p'\,\dot{q}' \approx \frac{1}{2}\,\mathrm{Re}\{P(\boldsymbol{x}, t)\; Q^*(\boldsymbol{x}, t)\}, \tag{2.5}$$

https://doi.org/10.1017/jfm.2026.11892 Published online by Cambridge University Press

where Re{·} denotes the real part. Consequently, the RI becomes

$$\mathcal{R}(\boldsymbol{x};\, T) = \frac{1}{2}\,\mathrm{Re}\left\{\frac{1}{T}\int_{t_0}^{t_0+T} P(\boldsymbol{x},\, t)\; Q^{*}(\boldsymbol{x},\, t)\,\mathrm{d}t\right\}. \tag{2.6}$$

This form shows that only the in-phase component of P and Q contributes to net thermoacoustic work.

2.1. *Dynamic mode decomposition-based reconstruction with acoustic scaling*

To evaluate the modal RI, DMD is applied to an acoustically scaled state vector. Direct use of raw fields means that the Euclidean norm is implicit in the single value decomposition bias mode selection toward variables of large numerical magnitude rather than toward an acoustically relevant dynamics. To emphasise thermoacoustic interactions, the state is restricted to pressure and heat release, scaled in analogy to Chu's acoustic energy norm (Chu 1965), which balances perturbation pressure and velocity. In the present configuration, dominated by monopole-like acoustic radiation, p' is expected to capture the essential acoustic dynamics with velocity fluctuations excited by the acoustic impedance relation. The resulting state vector is

$$\boldsymbol{y}(\boldsymbol{x},\, t) = \begin{bmatrix} \tilde{p}(\boldsymbol{x},\, t) \\ \tilde{q}(\boldsymbol{x},\, t) \end{bmatrix}, \tag{2.7}$$

with

$$\begin{aligned} \tilde{p}(\boldsymbol{x},\, t) &= \frac{p'(\boldsymbol{x},\, t)\,\sqrt{\Delta V(\boldsymbol{x})}}{\sqrt{\bar{\rho}(\boldsymbol{x})}\,\bar{c}(\boldsymbol{x})}, \\ \tilde{q}(\boldsymbol{x},\, t) &= \frac{(\gamma-1)\,\dot{q}'(\boldsymbol{x},\, t)\,\sqrt{\Delta V(\boldsymbol{x})}}{\bar{\rho}(\boldsymbol{x})\,\bar{c}^{2}(\boldsymbol{x})}, \end{aligned} \tag{2.8}$$

where γ is the heat capacity ratio, ΔV is the cell volume and $\bar{\rho}$ and $\bar{c}$ are the local mean density and sound speed, respectively. The pressure scaling corresponds to Chu's normalisation, while the heat-release term provides a pressure-like source consistent with the acoustic energy balance. This choice represents the isentropic subset of Chu's disturbance energy, while inclusion of kinetic and entropy terms would additionally require reliable $\boldsymbol{u}'$ and s' fields. Thus, the acoustic-subset normalisation biases DMD toward a compressive (acoustic) dynamics, such that the retained modes are predominantly acoustic, although some near-field reactive (pseudo-sound) contribution to p' may persist. Therefore, the resulting scalars are best interpreted as modal ranking and radiation trends rather than as absolute acoustic power. Applying the same methodology to a fully resolved acoustic perturbation equation (APE) (Geiser *et al.* 2014) field would circumvent this limitation and is left for future work.

Applying DMD to $\boldsymbol{y}(\boldsymbol{x},\, t)$ yields a set of K spatio-temporal modes. The analytic reconstructions of the pressure and heat-release signals take the form

$$P(\boldsymbol{x},\, t) = \sum_{k=1}^{K} \hat{p}_k(\boldsymbol{x})\,\mathrm{e}^{\lambda_k t}, \tag{2.9}$$

$$Q(\boldsymbol{x},\, t) = \sum_{k=1}^{K} \hat{q}_k(\boldsymbol{x})\,\mathrm{e}^{\lambda_k t}, \tag{2.10}$$

https://doi.org/10.1017/jfm.2026.11892 Published online by Cambridge University Press

where $\lambda_k = \sigma_k + \mathrm{i}\,\omega_k$ is the complex eigenvalue of mode k, with temporal growth rate σ_k and angular frequency ω_k. The modal coefficients (DMD amplitudes) b_k weight the spatial eigenfunctions, yielding $\hat{p}_k(\boldsymbol{x}) = b_k\,\phi_{p,k}(\boldsymbol{x})$ and $\hat{q}_k(\boldsymbol{x}) = b_k\,\phi_{q,k}(\boldsymbol{x})$, where b_k is the DMD amplitude associated with mode k. The quadratic interaction PQ^* yields

$$PQ^* = \sum_{k=1}^{K}\sum_{\ell=1}^{K} \hat{p}_k(\boldsymbol{x})\,\hat{q}_\ell^*(\boldsymbol{x})\,\mathrm{e}^{(\lambda_k+\lambda_\ell^*)t}. \tag{2.11}$$

Time averaging the modal exponential term $\mathrm{e}^{(\lambda_k+\lambda_\ell^*)t}$ over the window $[0,\ T]$ yields

$$J_{k\ell}(T) = \frac{\mathrm{e}^{(\lambda_k+\lambda_\ell^*)T} - 1}{T\,(\lambda_k + \lambda_\ell^*)}, \tag{2.12}$$

which quantifies the finite-time coupling between modes k and ℓ.

Plugging (2.11) into (2.6), the modal RI reads in closed form

$$\mathcal{R}(\boldsymbol{x};\,T) = \frac{1}{2}\,\mathrm{Re}\left\{\sum_{k=1}^{K}\sum_{\ell=1}^{K} \hat{p}_k(\boldsymbol{x})\,\hat{q}_\ell^*(\boldsymbol{x})\,J_{k\ell}(T)\right\}. \tag{2.13}$$

Equation (2.13) reveals that the RI admits a natural modal decomposition. The diagonal terms ($k = \ell$) represent the self-coupling of each DMD mode, while the off-diagonal terms ($k \neq \ell$) quantify cross-modal interactions. The latter decay as $|J_{k\ell}(T)| \to 0$ when the averaging window is large compared with the modal beat period. However, if it persists for a finite T it causes cross-modal leakage.

2.2. *Modal and cross-modal contributions*

The kernel $J_{k\ell}(T)$ defined in (2.12) governs the finite-time coupling between pressure and heat-release modes. For self-interactions ($k = \ell$), the kernel simplifies to

$$J_{kk}(T) = \frac{\mathrm{e}^{2\sigma_k T} - 1}{2\sigma_k T} \;\equiv\; F(\sigma_k,\,T), \tag{2.14}$$

which reduces smoothly to $J_{kk}(T) \to 1$ as $\sigma_k \to 0$. The resulting mode-specific Rayleigh density is

$$\mathcal{R}_k(\boldsymbol{x};\,T) = \frac{1}{2}\,F(\sigma_k,\,T)\,\mathrm{Re}\big\{\hat{p}_k(\boldsymbol{x})\,\hat{q}_k^*(\boldsymbol{x})\big\}. \tag{2.15}$$

Equation (2.15) shows that each DMD mode contributes independently through the in-phase product $\hat{p}_k\hat{q}_k^*$. The factor $F(\sigma_k, T)$ corrects for exponential growth or decay over the averaging window.

For cross-interactions ($k \neq \ell$), the kernel becomes in the neutral limit ($\sigma_k \approx \sigma_\ell \approx 0$)

$$J_{k\ell}(T) = \frac{\mathrm{e}^{i\,(\omega_k-\omega_\ell)T} - 1}{\mathrm{i}\,(\omega_k - \omega_\ell)T} = \mathrm{e}^{\,i\,\dfrac{\Delta\omega\,T}{2}}\ \mathrm{sinc}\!\left(\tfrac{\Delta\omega\,T}{2}\right), \tag{2.16}$$

with $\Delta\omega = \omega_k - \omega_\ell$. The leakage magnitude $|\mathrm{sinc}(\Delta\omega T/2)|$ quantifies the strength of residual coupling between distinct modes. It decays as the Rayleigh window T grows relative to the modal beat period $2\pi/|\Delta\omega|$, but remains finite when the window is short or frequencies are closely spaced. This behaviour is illustrated in figure 1, which shows how leakage decreases with increasing window length and with neighbour rank r, i.e. frequency separation in multiples of the fundamental spacing. In particular, when $T_{Rayleigh} = T_{DMD}$

https://doi.org/10.1017/jfm.2026.11892 Published online by Cambridge University Press

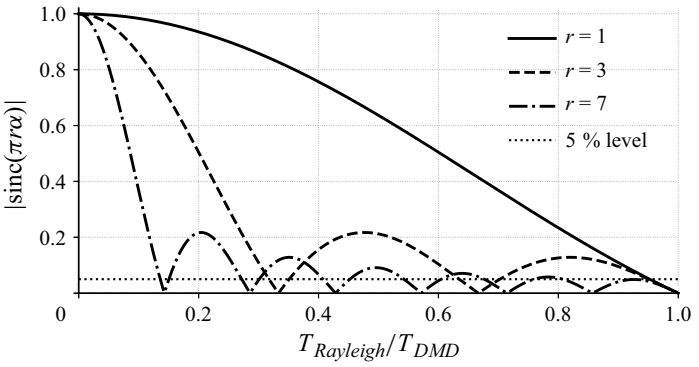


Figure 1. Magnitude of cross-modal leakage $|\mathrm{sinc}(\pi r\alpha)|$ as a function of the relative Rayleigh window length $\alpha = T_{Rayleigh}/T_{DMD}$. The parameter r denotes the neighbour rank, i.e. the frequency separation in multiples of the fundamental spacing. Larger r corresponds to more distant modal neighbours. The dotted line indicates the 5 % threshold.

and the modal frequencies lie on a perfect harmonic grid, $\Delta\omega T$ is an integer multiple of 2π, so the sinc term vanishes exactly and cross-modal leakage is eliminated.

When growth or decay exists, cross-interactions persist even under grid alignment. For general growth rates σ_k, σ_ℓ, the exact kernel for a rectangular window $[0, T]$ reads $a = \sigma_k + \sigma_\ell$ and $b = \Delta\omega$

$$J_{k\ell}^{[0,T]} = \frac{\mathrm{e}^{(a+\mathrm{i}b)T} - 1}{T\,(a + \mathrm{i}b)}. \tag{2.17}$$

The magnitude is

$$\left|J_{k\ell}^{[0,T]}\right| = \frac{\mathrm{e}^{aT/2}}{T\,\sqrt{a^2 + b^2}}\,\sqrt{2[\cosh(aT) - \cos(bT)]}\,. \tag{2.18}$$

This reduces to the sinc form when $a \to 0$. However, for grid-aligned frequencies ($bT = 2\pi m$, $m \in \mathbb{Z}$) and non-zero a, the leakage remains finite

$$\left|J_{k\ell}^{[0,T]}\right| = \frac{\mathrm{e}^{aT} - 1}{T\,\sqrt{a^2 + b^2}} \approx \frac{|a|}{|b|} \quad \text{if} \quad |a| \ll |b|. \tag{2.19}$$

Thus, exponential growth or decay breaks strict orthogonality of the modal expansion, leaving a residual cross-contribution even on a perfect grid.

2.3. *Scalar modal RI*

The total contribution of a single mode can be determined by integrating the local modal RI (2.15) over the domain volume V. In a discretised setting with cell volumes ΔV_i, this yields

$$R_k(T) = \frac{1}{2}\,F(\sigma_k, T)\,\mathrm{Re}\left\{\sum_i \hat{p}_k(\boldsymbol{x}_i)\,\hat{q}_k^*(\boldsymbol{x}_i)\,\Delta V_i\right\}. \tag{2.20}$$

For the neutrally stable case ($\sigma_k \approx 0$), the prefactor reduces to $F(\sigma_k, T) = 1$. If, in addition, the Rayleigh window is chosen equal to the DMD data span ($T = T_{DMD}$), cross-modal leakage vanishes (see figure 1). Under these conditions, the expression simplifies to

https://doi.org/10.1017/jfm.2026.11892 Published online by Cambridge University Press

the purely diagonal form

$$\mathcal{R}_k(\boldsymbol{x}) = \frac{1}{2}\,\mathrm{Re}\big\{\hat{p}_k(\boldsymbol{x})\,\hat{q}_k^*(\boldsymbol{x})\big\}, \tag{2.21}$$

and the corresponding scalar RI becomes

$$R_k = \frac{1}{2}\,\mathrm{Re}\left\{\sum_i \hat{p}_k(\boldsymbol{x}_i)\,\hat{q}_k^*(\boldsymbol{x}_i)\,\Delta V_i\right\}. \tag{2.22}$$

This reduced form is particularly convenient for practical analysis. It provides mode-wise Rayleigh maps that are uncontaminated by cross-terms and allows direct ranking of the modal contributions to thermoacoustic excitation or energy absorption.

2.4. *Quadrature pressure–heat-release correlation*

The modal RI R_k quantifies the in-phase work between pressure and unsteady heat release and thereby ranks each mode as a feedback-effective source ($R_k > 0$) or sink ($R_k < 0$) of acoustic energy. Unsteady heat release also appears as a source term in the acoustic wave equation

$$\frac{1}{c_0^2}\,\partial_t^2 p' - \nabla^2 p' \;=\; \frac{\gamma_0 - 1}{c_0^2}\,\partial_t \dot{q}' \;+\; \ldots, \tag{2.23}$$

such that in the compact-source limit ($kL \to 0$) the far-field pressure p_{ff} at distance r reads

$$p_{ff}(t) \;\approx\; \frac{\gamma_0 - 1}{4\pi c_0^2 r}\,\frac{d}{\mathrm{d}t}\,\dot{q}'\Big(t - \tfrac{r}{c_0}\Big)\,. \tag{2.24}$$

For a harmonic $\dot{q}'(t) = \mathrm{Re}\{\hat{q}\,\mathrm{e}^{i\omega t}\}$, temporal differentiation yields $(d/\mathrm{d}t)\dot{q}' = \mathrm{Re}\{\mathrm{i}\omega\hat{q}\,\mathrm{e}^{i\omega t}\}$. In this idealised limit, the far field is shifted by $+90°$ relative to $\dot{q}'$. This motivates using p–$\dot{q}$ quadrature as a signature of source activity in the compact-source limit ($kL \to 0$) only.

Within a modal (DMD) representation, the period average of p' times the source term in (2.23) yields the modal source-term weighting

$$w_k(\boldsymbol{x}) = \frac{\gamma_0(\boldsymbol{x}) - 1}{c_0(\boldsymbol{x})^2}\,\frac{\omega_k}{2}\,\mathrm{Im}\big\{\hat{p}_k(\boldsymbol{x})\,\hat{q}_k(\boldsymbol{x})^*\big\}\,, \tag{2.25}$$

which depends on the imaginary part of the local p–$\dot{q}$ correlation. This motivates a window-consistent quadrature companion to the Rayleigh map

$$Q_k^{\perp}(T) = \frac{1}{2}\,F(\sigma_k, T)\sum_i \mathrm{Im}\big\{\hat{p}_k(\boldsymbol{x}_i)\,\hat{q}_k(\boldsymbol{x}_i)^*\big\}\;\Delta V_i, \tag{2.26}$$

with the finite-time factor F.

Large $\mathcal{R}_k(\boldsymbol{x}; T) = (1/2)F\,\mathrm{Re}\{\hat{p}_k\hat{q}_k^*\}$ marks regions where the in-phase coupling drives ($R_k > 0$) or absorbs ($R_k < 0$) acoustic energy ($R_k \propto \mathrm{Re}S_k$), whereas large $\mathrm{Im}\{\hat{p}_k\hat{q}_k^*\}$ highlights quarter-cycle-shifted coupling associated with the source term in (2.23). In the strict compact-source limit ($kL \to 0$), the spatially integrated quadrature is proportional to far-field monopole output and with the $\mathrm{e}^{i\omega t}$ convention the pressure leads HRR by $+90°$.

However, real flames generally differ from that limit. Convective transport imposes distributed delays $\tau(\boldsymbol{x})$ such that $\phi(\boldsymbol{x}) \approx -\omega_k\tau(\boldsymbol{x})$ (Schuller *et al.* 2003; Polifke 2020). Acoustic mode shapes imprint spatially varying pressure phase and near-field reactive contributions imply that not all pressure fluctuations correspond to far-field sound (Ffowcs

https://doi.org/10.1017/jfm.2026.11892 Published online by Cambridge University Press

Williams 1969; Fahy & Gardonio 2003; Pierce 2019). These effects generate positive and negative patches in quadrature maps and the volume-integrated $Q_k^{\perp}(T)$ can even be negative if lagging regions dominate.

To obtain a phase-invariant measure of coupling magnitude, we define

$$Q_k^{eff}(T) = \frac{1}{2}\, F(\sigma_k, T)\, \left| \sum_i \hat{p}_k(\boldsymbol{x}_i)\, \hat{q}_k(\boldsymbol{x}_i)^*\, \Delta V_i \right| = \frac{1}{2}\, F(\sigma_k, T)\, |S_k|, \tag{2.27}$$

that is, the magnitude of the spatially integrated p–HRR cross-spectrum for mode k. The triplet

$$R_k(T) = \frac{1}{2}\, F\, \mathrm{Re} S_k, \qquad Q_k^{eff}(T) = \frac{1}{2}\, F\, |S_k|, \qquad \phi_k^* = \arg S_k, \tag{2.28}$$

with $S_k = \sum_i \hat{p}_k \hat{q}_k^*\, \Delta V_i$, separates (i) in-phase work (feedback excitation/absorption), (ii) phase-invariant coupling magnitude and (iii) the global phase offset. In an externally forced, effectively anechoic configuration, $Q_k^{\perp}$ and Q_k^{eff} should be interpreted as coupling metrics. Quadrature primarily reflects reactive or transport-induced phase structure rather than far-field radiation. Therefore, the sign of $Q_k^{\perp}$ is not, by itself, diagnostic of radiated output. The phase-invariant efficiency $Q_k^{eff} \propto |S_k|$ complements R_k by measuring the mode-weighted coupling magnitude irrespective of absolute phase. A useful sensitivity relation is $\partial R_k / \partial \phi_k = -\,\mathrm{Im} S_k$. It shows that regions/modes with large quadrature are highly responsive to small phase changes. More generally, for perturbations of the parameter vector $\boldsymbol{\theta} = (\phi, U_{in}, T_{in}, \ldots)$

$$\mathrm{d}R_k = (\mathrm{d}|S_k|) \cos\phi_k \; - \; |S_k| \sin\phi_k \; (\mathrm{d}\phi_k). \tag{2.29}$$

Hence, changes in spatial coherence/gain (via $\mathrm{d}|S_k|$) and in phase ($\mathrm{d}\phi_k$) both affect R_k. This framework is applied in §§ 3 and 4 to acoustically forced lean H_2–air slit flames in which thermodiffusively unstable intrinsic modes co-exist with externally driven modes across overlapping frequency ranges, providing the multi-modal environment in which frequency-resolved, mode-specific thermoacoustic analysis is most informative.

3. Numerical methods and simulation set-up

The flow field evolution is governed by the fully compressible Navier–Stokes equations for reacting flows (Poinsot & Veynante 2005). A conservative finite-volume formulation is applied for spatial discretisation. Variables at cell interfaces are reconstructed using the monotonic upstream-centered scheme for conservation laws scheme for conservation laws (van Leer 1979). Convective fluxes are obtained with a modified advection upstream splitting method (Liou & Steffen 1993), while viscous terms are approximated through central differencing. Time advancement is performed using a five-stage Runge–Kutta algorithm optimised for stability.

Temperature-dependent heat capacities are evaluated using NASA7 polynomial coefficients (McBride *et al.* 1993). The mixture-averaged diffusion model is employed, with thermal diffusion effects for hydrogen (H and H_2) incorporated following the procedure described in Schlup & Blanquart (2018). Validation of the reacting-flow solver and the reduced Soret formulation is reported in the supplementary material https://doi.org/10.1017/jfm.2026.11892, and in Beltran *et al.* (2022). Chemical kinetics are based on Kee *et al.* (2018) using the Li *et al.* (2004) mechanism with 9 species and 19 reactions.

To handle the stiffness arising from the disparity between chemical and transport time scales (Lu & Law 2009) efficiently, an operator-splitting approach is employed.

https://doi.org/10.1017/jfm.2026.11892 Published online by Cambridge University Press

Case type	ϕ	Excitation [Hz]	Notes	No. of Simulations
Baseline	0.4	—	No excitation	—
	0.5	—	No excitation	4
	0.6	—	No excitation	—
	0.7	—	No excitation	—
Single frequency	0.4	220, 437, 800	Single-tone; separate runs	—
	0.5	220, 437, 800	Single tone; separate runs	12
	0.6	220, 437, 800	Single tone; separate runs	—
	0.7	220, 437, 800	Single tone; separate runs	—
Multi-frequency	0.4	mf_0, $m = 1 \ldots 22$	Multi-tone in one run	—
	0.5	mf_0, $m = 1 \ldots 22$	Multi-tone in one run	4
	0.6	mf_0, $m = 1 \ldots 22$	Multi-tone in one run	—
	0.7	mf_0, $m = 1 \ldots 22$	Multi-tone in one run	—

Table 1. Summary of conducted simulation cases for several equivalence ratios ϕ, excitation types and forcing set-ups. For multi-frequency cases, $f_0 = 50$ Hz.

Chemical kinetics are handled by coupling `pyJac` (Niemeyer *et al.* 2017) with `SUNDIALS` (Hindmarsh *et al.* 2005). This approach ensures efficient execution on both CPU and GPU platforms, supporting CUDA and HIP backends. The use of `pyJac`'s analytical Jacobian accelerates the evaluation of reaction rate source terms by a factor of 5–10 compared with finite-difference approximations, as demonstrated in prior studies for hydrogen and related systems (Tekgül *et al.* 2021; Haider *et al.* 2025). Transport is advanced within the multiphysics framework m-AIA (multiphysics-Aerodynamisches Institut Aachen) (Institute of Aerodynamics 2024). The accuracy of the overall numerical approach has been shown in Schlimpert *et al.* (2016) and Herff *et al.* (2020).

To investigate the inherent instabilities of hydrogen flames and the related acoustic emissions, two-dimensional simulations of a laminar slit are conducted. Simulations are performed for four fuel–air equivalence ratios $\phi = \{0.4, 0.5, 0.6, 0.7\}$. A summary of the performed cases can be found in table 1. The chosen equivalence ratio range is representative of practical lean-premixed hydrogen combustion. Even the richer cases considered ($\phi = 0.6$, $\phi = 0.7$) achieve significant NO_x reductions, reaching values several orders of magnitude lower than in stoichiometric flames (Correa 1993). Acoustic excitation is applied by imposing a sinusoidal signal to the inlet velocity at three frequencies $f_{exc} = \{220, 437, 800\}$ Hz with a fixed amplitude of $\varepsilon = 0.05$ with respect to the mean inlet velocity. The flame response to the perturbations is analysed and compared with the baseline cases, i.e. the non-excited cases. Four additional simulations are performed using a multi-frequency forcing signal, where the inlet velocity perturbations are expressed as a combination of harmonic components. Each component is an integer multiple of the fundamental frequency $f_0 = 50$ Hz

$$u' = \varepsilon\, \bar{u} \sum_m \sin(2\pi f_0 m t), \tag{3.1}$$

with $m \in \{1, 2, \ldots, 22\}$. To minimise nonlinear effects, the relative fluctuation amplitude of the perturbation signal is limited to $\varepsilon = 0.005$ with respect to the mean inlet velocity (Rodríguez-Pastor *et al.* 2024). This formulation excites all harmonics simultaneously, allowing DMD to resolve the coherent modal dynamics across the full frequency range from a single simulation. Because all tones are integer multiples of f_0, nonlinear intermodulation products coincide with the excitation frequencies. This overlap makes classical FTF extraction ambiguous, but does not affect the DMD–Rayleigh analysis: the

https://doi.org/10.1017/jfm.2026.11892 Published online by Cambridge University Press

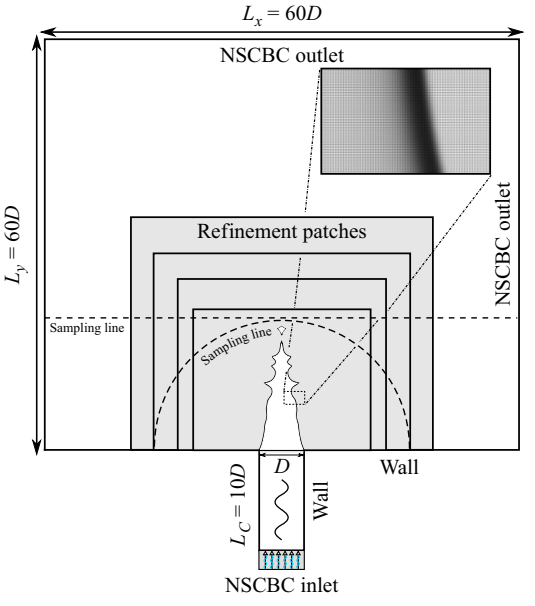


Figure 2. Computational domain of the slit flame. Inlet (bottom) and outlets (top, left, right) are given as NSCBCs. The grid is refined in the vicinity of the flame, with gradually decreasing mesh refinement levels further off the flame.

method identifies the coherent structures at each frequency regardless of their origin, whether from the direct forced response, from interactions between tones or from the intrinsic TD instability of the flame. For flames that respond linearly, the multi-tone approach yields frequency-response estimates consistent with single-tone simulations (Rodríguez-Pastor *et al.* 2024).

All simulations are conducted at a constant ratio of inlet velocity to laminar flame speed, $u_\infty/s_L = 6.0$. This ensures that the flame length remains comparable across equivalence ratios. More fundamentally, fixing u_∞/s_L maintains comparable dimensionless flow and stretch conditions. For a steady slit flame, the kinematic balance $s_L = u_\infty \sin\alpha$ links the cone angle α to u_∞/s_L, while the local stretch scales as $K \sim s_L/D + u_\infty/D$ for channel width D. With u_∞/s_L fixed, both contributions are of the same order, yielding a dimensionless stretch $\chi = K\delta_L/s_L \sim (1 + C)\,\delta_L/D$ that is primarily controlled by geometry and varies mainly through the mixture-dependent δ_L/D. Consequently, the stretch response $s_n/s_L \approx 1 - Ma\,\chi$, where Markstein number Ma, varies with equivalence ratio mainly through changes in Ma and mixture properties, rather than through geometric effects. On the other hand, for a fixed forcing frequency, $St_f = f D/u_\infty$ and the inlet Reynolds number drift with $s_L(\phi)$.

All simulations are performed at ambient temperature and pressure of 291 K and 1 bar. The temporal resolution is chosen according to the acoustic Courant–Friedrichs–Lewy (CFL) stability condition, resulting in a time step of approximately $\Delta t \approx 3 \times 10^{-8}$ s for all cases, with slight case-to-case variations as richer mixtures yield hotter burnt gases and thus higher local sound speeds, which impose the most restrictive CFL limit.

The computational domain shown in figure 2 includes the entire inlet plenum and upstream channel, to make sure that inlet perturbations and its effects are fully resolved (Herff *et al.* 2020). The dimensions of the domain are $L_x = L_y = 60D$, where $D = 1$ cm

https://doi.org/10.1017/jfm.2026.11892 Published online by Cambridge University Press

denotes the channel width. This means that the distance between the flame and the boundaries suffices to suppress non-physical interactions.

To prevent artificial pressure wave reflections, Navier–Stokes characteristic boundary conditions (NSCBCs) (Poinsot & Lele 1992; Lodato *et al.* 2008) are applied to all inlet and outlet boundaries. These non-reflecting conditions minimise the formation of spurious standing waves that could otherwise interfere with the flame dynamics and distort the development of intrinsic instabilities.

Local grid refinement is used near the flame to resolve steep gradients in the reaction zone, while a coarser mesh is employed in the far field. The flame front is resolved by at least 15 cells across the flame for all cases. Sampling lines are placed both along the flame front and in the acoustic field to monitor HRR fluctuations and pressure signals.

4. Results

Before applying the modal Rayleigh framework derived in § 2, it is first necessary to characterise the baseline physical dynamics of the flame. While the acoustic response of perfectly stable laminar methane–air flames is well documented in the literature (Candel 2002; Durox *et al.* 2009), lean hydrogen–air flames exhibit strong intrinsic TD instabilities. Consequently, external acoustic forcing does not merely impose a linear perturbation, it actively competes and interacts with the flame's natural cellular structures. Sections 4.1 to 4.5 document these physical interactions, i.e. cell-size redistribution, nonlinear harmonic generation and acoustic radiation, providing the physical reference against which the DMD-based modal Rayleigh method is assessed in § 4.6, in an environment where forced and intrinsic dynamics coexist.

The characterisation begins with the morphological response of the flame to acoustic forcing. Instantaneous snapshots of the non-excited and excited flames are presented in figure 3(*a*), showing the HRR together with temperature fields. The corresponding time-averaged fields are displayed in figure 3(*b*) using the OH mass fraction (Y_{OH}) as a marker. For the leanest mixture ($\phi = 0.4$), intrinsic instabilities are already visible in the non-excited flame. Under excitation at 220 and 437 Hz, the flame shortens and develops large cellular structures, whereas at 800 Hz smaller-scale wrinkles dominate and the flame is stretched. This behaviour is confirmed by the averaged OH contours, where the flame appears longer at the highest frequency. For $\phi = 0.4$ and $\phi = 0.5$, excitation at higher frequencies (437 and 800 Hz) produces the most pronounced changes, with enhanced cellular structures leading to a shorter mean flame length. A comparable trend is also observed for $\phi = 0.7$, although the flame morphology differs substantially for the 437 and 800 Hz cases, indicating a strong frequency-dependent response.

4.1. *Cell-size distribution*

The probability density functions (PDFs) of the normalised flame cell size λ_{cell}/l_f for $\phi = 0.4, 0.5, 0.6, 0.7$ and excitation frequencies $f_{exc} = 0, 220, 437, 800$ Hz are shown in figure 4. Following Berger *et al.* (2019), the smallest cell size λ_{cell} is defined as the distance between two adjacent cusp tips. Assuming a semicircular shape for the flame front between cusps, λ_{cell} can be expressed as $\lambda_{cell} = 2l^*/\pi$, where l^* is the arc length between two curvature peaks along the flame front. The curvatures are identified over the isoline of the progress variable $C = T - T_\infty/T_{ad} - T_\infty = 0.5$. Berger *et al.* (2019) characterised the natural cell-size selection in thermodiffusively unstable hydrogen flames evolving under intrinsic instability alone. The present analysis extends this by examining how external acoustic forcing alters these distributions across different equivalence ratios and frequencies.

https://doi.org/10.1017/jfm.2026.11892 Published online by Cambridge University Press

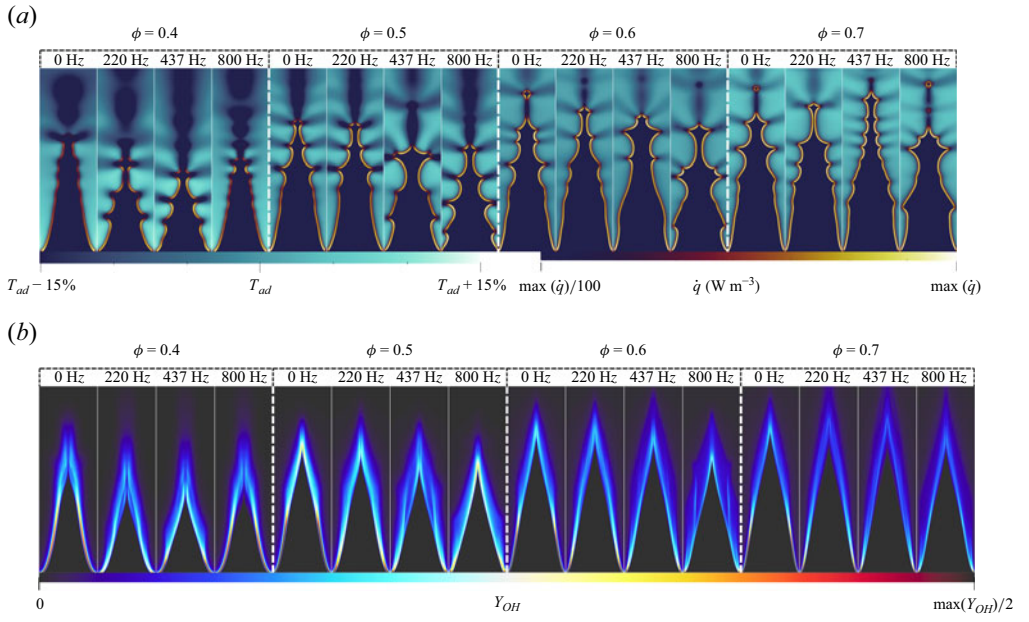


Figure 3. (*a*) Heat release rate ($\dot{q}$) at the flame front and temperature field contours for four cases at different fuel–air equivalence ratios (ϕ). From left to right: $\phi = 0.4$, 0.5, 0.6, 0.7, with each equivalence ratio including four excitation frequencies ($f_{exc} = 0$, 220, 437 and 800 Hz). (*b*) Mean OH mass fraction for the same four cases, with the same equivalence ratios and excitation frequencies.

In all cases, the non-excited flames ($f_{exc} = 0$ Hz) already exhibit cellular structures which are consistent with the intrinsic instability of hydrogen–air slit flames. For the leanest mixture ($\phi = 0.4$), the non-excited distribution is dominated by small cell sizes $\lambda_{cell}/l_f \approx 3$–5. External excitation largely reinforces this mode. For $f_{exc} = 800$ Hz an even stronger probability concentration at the smallest scales is observed. At $\phi = 0.5$, the non-excited case peaks at intermediate sizes $\lambda_{cell}/l_f \approx 5$–8 and excitation broadens the distribution. Notably, the $f_{exc} = 800$ Hz case deviates from the behaviour for $\phi = 0.4$ by producing a secondary mode at larger scales. This indicates that high-frequency forcing can promote growth of larger cells instead of suppressing them. At $\phi = 0.6$, the non-excited distribution is already wider. Excitation introduces bimodality. While the case with $f_{exc} = 220$ Hz remains close to the baseline, excitation at $f_{exc} = 800$ Hz enhances the large-size tail $\lambda_{cell}/l_f > 12$, which again contradicts the expectation that higher frequency would preferentially stabilise small-scale cells. Finally, for the richest case $\phi = 0.7$, the non-excited distribution is strongly biased toward larger scales. However, the effect of excitation is non-intuitive, the intermediate frequency $f_{exc} = 437$ Hz enhances a smaller-cell mode in the range $\lambda_{cell}/l_f \approx 6$–7, while the high-frequency case $f_{exc} = 800$ Hz pushes the distribution further toward larger scales.

Overall, these results demonstrate that external acoustic forcing fundamentally alters the cell-size distributions compared with the intrinsic TD patterns documented by Berger *et al.* (2019). Critically, the response is highly non-monotonic: the same forcing frequency (e.g. 800 Hz) can enhance small-scale structures at $\phi = 0.4$, promote bimodality at $\phi = 0.5$–0.6 or drive the distribution toward larger scales at $\phi = 0.7$. This equivalence-ratio-dependent behaviour suggests that acoustic perturbations actively compete with intrinsic TD wavelength selection, rather than simply modulating the amplitude of naturally occurring

https://doi.org/10.1017/jfm.2026.11892 Published online by Cambridge University Press

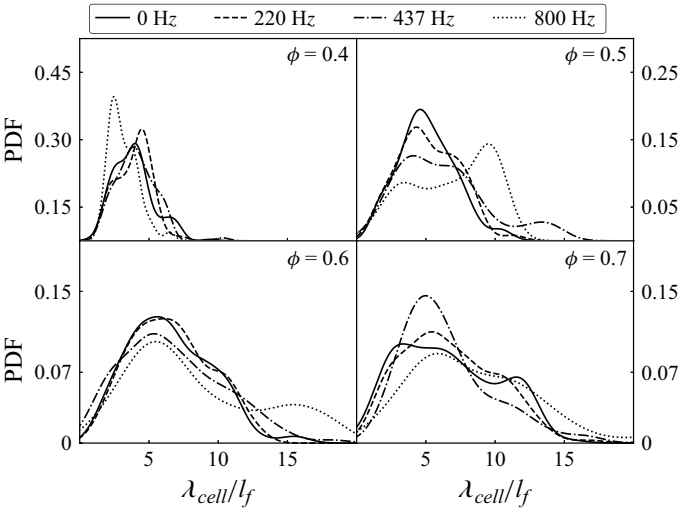


Figure 4. Probability density functions of the normalised flame cell size λ_{cell}/l_f for various equivalence ratios ($\phi = 0.4$, 0.5, 0.6, 0.7) under different excitation frequencies $f_{exc} = 0$, 220, 437 and 800 Hz.

cellular patterns. The interaction outcome depends on the balance between forcing time scale, chemical time scale and the most-amplified intrinsic wavelength: a balance that shifts systematically with mixture composition. The spatial redistribution of cell sizes shown in figure 3(*a*) indicates that the flame does not respond linearly to acoustic forcing: different frequencies selectively amplify different spatial scales, and in some cases produce entirely new (bimodal) distributions through interactions between intrinsic and forced modes. This spatial nonlinearity manifests as temporal distortion when wrinkles of varying size convect through the flame, generating spectral content beyond the forcing frequency. We next quantify this through harmonic analysis of the integrated flame response.

4.2. *Nonlinear response and harmonic distortion*

The harmonic spectra of the flame response to periodic forcing are presented in figure 5 with normalised amplitudes of higher harmonics plotted relative to the fundamental amplitudes. Each panel corresponds to a different forcing frequency and equivalence ratio. The total harmonic distortion (THD) is defined as

$$\mathrm{THD} = \frac{\sqrt{\sum_{k=2}^{N} Q_k^2}}{Q_1}, \tag{4.1}$$

where Q_1 is the amplitude of the fundamental component of the integrated heat-release signal $q(t)$ at the excitation frequency f_{exc}, and Q_k is the amplitude of the kth harmonic. Across all conditions, the spectra are dominated by the second and third harmonics, with higher-order contributions decaying in amplitude. This shows that, while the flame response largely tracks the forcing frequency, nonlinear interactions lead to distinct harmonic generation. The impact of this nonlinearity expressed by THD varies systematically. In some cases, the response remains linear with limited harmonic content, while in others significant higher-order contributions broaden the spectrum and increase THD. Overall, the results demonstrate that the flame dynamics ranges from weakly to

https://doi.org/10.1017/jfm.2026.11892 Published online by Cambridge University Press

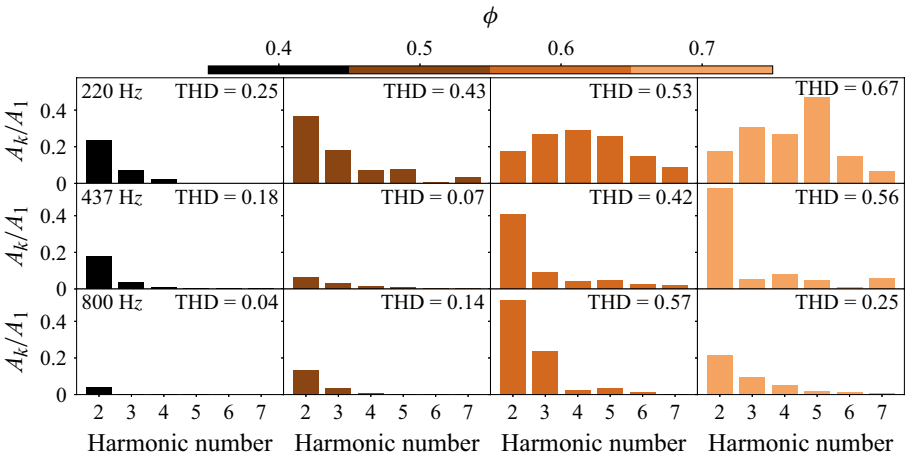


Figure 5. Harmonic spectra of the flame response showing normalised harmonic amplitudes and THD. The forcing frequency f_{exc} is constant for each row.

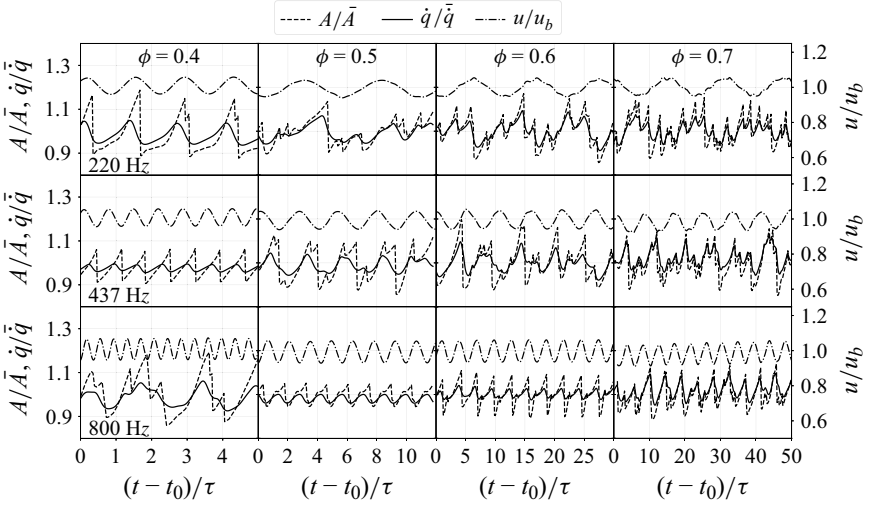


Figure 6. Temporal evolution of the normalised total HRR $\dot{q}/\bar{\dot{q}}$, total flame surface area $A/\bar{A}$ and inlet flow velocity u/u_b for the four flames at equivalence ratios $\phi = 0.4, 0.5, 0.6, 0.7$ (columns) excitation frequencies 220, 437, 800 Hz (rows). The quantity t_0 denotes the transient time during which the flame adapts to the excitation and τ represents the characteristic flame time scale.

strongly nonlinear depending on the operating conditions. Richer mixtures and lower forcing frequencies generally favour stronger nonlinear behaviour.

4.3. *Acoustic cycle*

To assess how the flame dynamics follows the excitation, figure 6 shows the imposed harmonic velocity at the channel exit centreline, normalised by the mean velocity at the same location, together with the corresponding responses in flame area and heat-release rate. At low to intermediate frequencies 220 and 437 Hz, the lean flame responds almost linearly, i.e. A and $\dot{q}$ remain synchronised with the excitation. More precisely, $\dot{q}$ is close to sinusoidal while A already shows mild non-sinusoidal features, so the response is phase

https://doi.org/10.1017/jfm.2026.11892 Published online by Cambridge University Press

locked but only weakly linear at lean ϕ. At higher enrichment, however, the response becomes increasingly nonlinear. While the flame remains phase locked to the excitation, the oscillations develop sharper peaks, asymmetry between rise and fall and cycle-to-cycle modulation, which lead to harmonic distortion. This distortion is most evident in A, which often exhibits a saw-tooth-like waveform with rapid drops and slower recovery, consistent with pocket shedding/cusp loss that abruptly removes flame surface, whereas $\dot{q}$ appears smoother.

At 800 Hz, the behaviour changes. In the lean case, the flame no longer follows the forcing but evolves on a much slower time scale with oscillations at periods three to four times longer than the excitation, combined with intermittent bursts. This reflects the fact that the forcing time scale $\tau_f \sim 1/f$ at 800 Hz $\phi = 0.4$ becomes comparable to or shorter than the chemical time scale τ_c, which is defined as the ratio of the laminar flame thickness to the laminar flame speed. When $\tau_f \lesssim \tau_c$, the heat release cannot adjust to the rapid oscillations, weakening direct coupling and allowing intrinsic hydrodynamic modes to dominate. In richer mixtures, however, the shorter chemical time scale allows the flame to remain locked to the 800 Hz forcing, although residual modulation of A and $\dot{q}$ indicates the persistence of secondary frequencies. Even in these richer cases, the flame surface area A retains stronger harmonic content than $\dot{q}$, in line with the waveform shapes in figure 6.

Overall, the results show that forcing frequency and equivalence ratio together set the balance between external synchronisation and intrinsic instabilities. Lean flames respond nearly linearly at low frequencies but decouple at high frequencies, while richer flames develop stronger harmonic distortion at low frequencies and remain locked at high frequencies. This is also evident from figure 7, which shows flame snapshots over a forcing cycle at different excitation frequencies. For some of the investigated conditions, the oscillation remains synchronised with the forcing, and the flame shape after 360° closely matches the initial phase. While this cycle-resolved analysis of the flame fields and integrated quantities such as heat release and flame area provides detailed insight into the internal response of the system, it does not capture the acoustic dynamics. To address this, we next examine the far-field acoustic response in terms of sound pressure level (SPL).

4.4. *Sound pressure level*

The acoustic output of the flame is quantified in terms of the SPL, defined relative to the reference pressure of 20 μPa. Figure 8 shows SPL spectra obtained from far-field pressure measurements for equivalence ratios $\phi = 0.4, 0.5, 0.6, 0.7$, for the non-excited reference configuration and the cases excited with frequencies 220, 437, 800 Hz. The analysis distinguishes between the natural combustion noise of the flame and the modifications introduced by external excitation. This provides a reference for how broadband laminar flame noise is reshaped into narrowband tonal responses as the equivalence ratio and forcing frequency are varied.

4.4.1. *Reference (non-excited) flame*

The non-excited SPL spectra shown as black curves in figure 8 provide a reference for the natural combustion noise of the flame. For the lean case $\phi = 0.4$, the spectrum exhibits broadband characteristics typical for laminar combustion noise, with elevated levels at low frequencies that decay gradually toward higher frequencies. In contrast, richer mixtures $\phi = 0.5, 0.6, 0.7$ radiate more strongly, particularly at low frequencies, although the spectra do not show any resonance effect. This behaviour is consistent with laminar premixed flames, which cannot sustain rapid heat-release fluctuations. No distinct tonal peaks are observed in the reference spectra, confirming the absence of acoustic resonances

https://doi.org/10.1017/jfm.2026.11892 Published online by Cambridge University Press

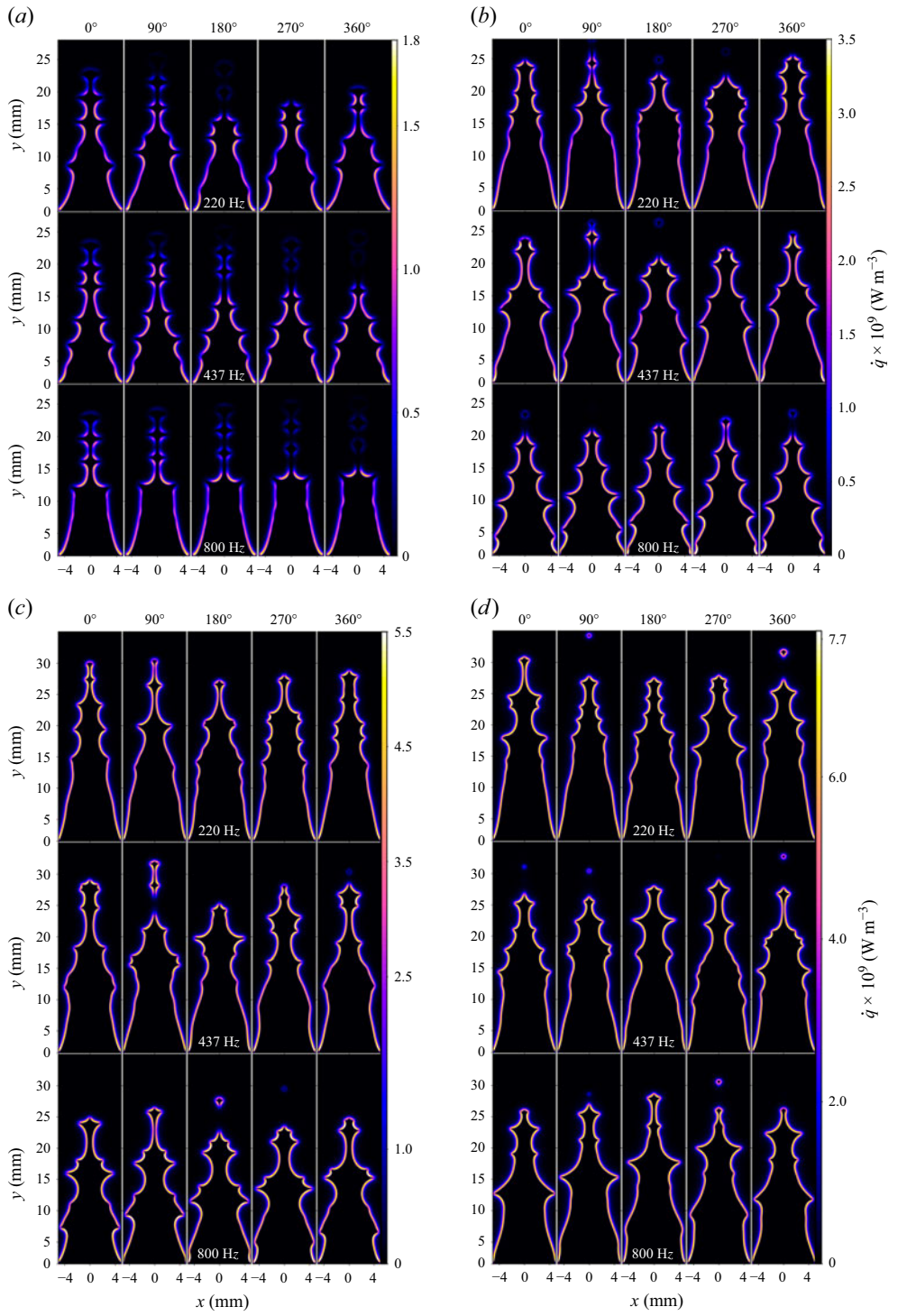


Figure 7. Flame HRR $\dot{q}$ fields at several phases 0°, 90°, 180°, 270° and 360° of the excitation cycles. Each subfigure corresponds to a different equivalence ratio case: (*a*) $\phi = 0.4$, (*b*) $\phi = 0.5$, (*c*) $\phi = 0.6$, (*d*) $\phi = 0.7$. Within each case, results are shown for excitation frequencies of 220, 437, 800 Hz. Full videos of the temporal evolution of the flames under external excitation are available as supplementary movies.

https://doi.org/10.1017/jfm.2026.11892 Published online by Cambridge University Press

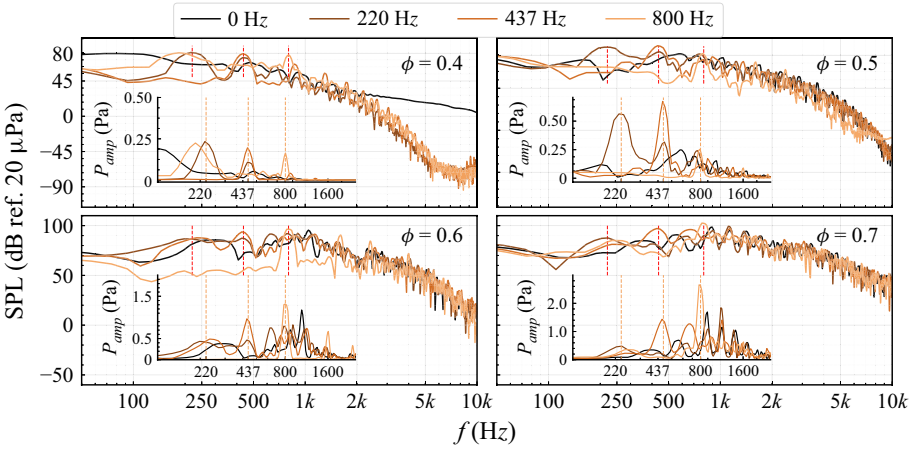


Figure 8. Sound pressure level spectra for $\phi = 0.4$, 0.5, 0.6, 0.7 flames under various excitation frequencies. The SPL (dB re 20 μPa) is plotted against frequency (Hz) on a logarithmic scale. Insets show the corresponding pressure amplitude spectra (P_{amp}). Vertical dashed lines indicate the applied excitation frequencies: 220, 437, 800 Hz.

in the open, anechoic set-up (Ihme & Pitsch 2012; Pausch *et al.* 2018). Nevertheless, distinct secondary features are visible across the spectra, which may reflect intrinsic flame dynamics or hydrodynamic–acoustic interactions.

4.4.2. *Forced flame spectra*

Harmonic forcing at discrete frequencies modifies the SPL spectra by generating narrowband peaks at the excitation frequency. However, figure 8 shows that the radiated response is not always centred at the excitation frequency itself. For the leanest flame $\phi = 0.4$, forcing at 800 Hz produces essentially no peak at the excitation frequency. Instead, a broad response appears near approximately 200 Hz, reflecting the fact that the flame cannot follow such rapid oscillations and radiates at a slower time scale defined by its intrinsic chemistry-transport dynamics. At $\phi = 0.5$, the flame responds more strongly at 220 and 437 Hz, but continues to show a relatively weak signature at 800 Hz, indicating limited coupling at that time scale. In contrast, the $\phi = 0.6$ flame couples at 437 and 800 Hz, with 800 Hz producing a sharp peak at the fundamental as well as visible harmonics, while the 220 Hz forcing excites primarily its second harmonic frequency near 440 Hz rather than the fundamental frequency. The richest case $\phi = 0.7$ possesses the highest overall SPL, but again the 220 Hz excitation does not dominate. Instead, energy appears more prominently at higher harmonics. This suggests that the external forcing does not fully suppress the flame's intrinsic dynamics, allowing energy to remain distributed among its natural oscillation modes.

Overall, the spectra demonstrate that the flame response reflects both the imposed forcing and the intrinsic time scales of heat-release fluctuations. In lean flames, high-frequency excitation leads either to slower responses ($\phi = 0.4$) or fails to couple altogether ($\phi = 0.5$). In richer flames, coupling is effective at 437 and 800 Hz, but 220 Hz excitation is largely redistributed into harmonic routes. The net effect is a selective concentration of acoustic energy into the driven frequencies and their harmonics. The strength of this redistribution increases with the equivalence ratio. These trends are consistent with the harmonic distortion analysis presented in figure 5, where richer flames $\phi = 0.6$, 0.7 exhibit clearly higher THD and stronger harmonic content. This confirms that part of

https://doi.org/10.1017/jfm.2026.11892 Published online by Cambridge University Press

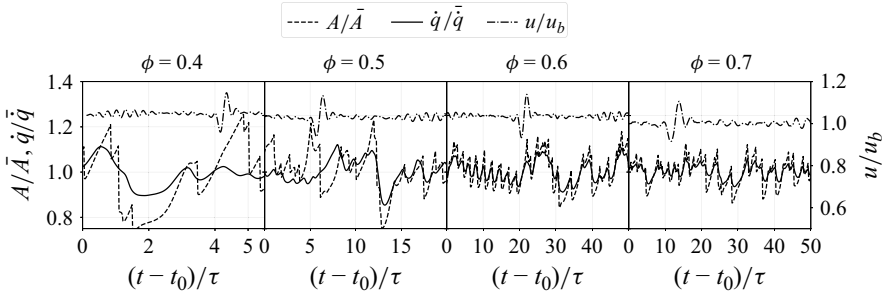


Figure 9. Temporal evolution of the normalised total HRR $\dot{q}/\bar{\dot{q}}_0$, total flame surface area $A/\bar{A}_0$ and inlet flow velocity u/u_b for the flames at equivalence ratios $\phi = 0.4, 0.5, 0.6, 0.7$ excited by a multi-frequency signal. The quantity t_0 denotes the transient time during which the flame adapts to the excitation and τ represents the characteristic flame time scale.

the excitation energy is systematically redistributed into harmonic routes rather than remaining confined to the excitation frequency.

4.5. *Multi-frequency SPL*

The temporal evolution of the normalised heat-release rate $\dot{q}/\bar{\dot{q}}_0$, flame surface area $A/\bar{A}_0$ and inlet velocity u/u_b under multi-frequency excitation is shown in figure 9. While the inlet velocity contains all 22 imposed tones between 100 and 1200 Hz, the flame does not track them uniformly. For the lean case $\phi = 0.4$, coupling to the high-frequency content is poor. Instead, the response exhibits irregular low-frequency modulations with alternating higher and lower amplitude cycles. This behaviour is consistent with the low-frequency bias inferred from the single-tone experiments (§ 4.4; cf. figure 6), where lean flames predominantly follow a slow dynamics. For the enriched mixture, high-frequency components have a more noticeable imprint on the flame dynamics, however, without a strictly periodic cycle. Overall, the flame behaves like a nonlinear filter, i.e. lean conditions emphasise the low-frequency content of the forcing, whereas richer mixtures reflect a mixed response in which intrinsic unsteadiness and high-frequency forcing interact. This behaviour is comparable to the results shown in figure 8.

Figure 10 illustrates the SPL spectra for flames at equivalence ratios $\phi = 0.4$ to $\phi = 0.7$ subjected to a multi-frequency excitation signal. The SPL spectra reveal a frequency-dependent response, with relatively stable response at low frequencies (50–200 Hz) transitioning to significant amplification in the high-frequency range (>1 kHz) which is particularly pronounced for richer flames $\phi = 0.7$. This trend is consistent with an upward shift of the effective flame cutoff $f_c(\phi)$ at increasing ϕ, which is also indicated by the single-tone results in figure 8. Beyond this cutoff shift, the emergence of energy at non-excitation frequencies indicates a nonlinear spectral redistribution by harmonics and intermodulation that is in line with dual-frequency observations in premixed flames (Zheng *et al.* 2024) and with general intermodulation behaviour (Noiray *et al.* 2008). The equivalence ratio dependence is particularly noteworthy. While the lean $\phi = 0.4$ case exhibits a controlled spectral response, the $\phi = 0.7$ case shows pronounced high-frequency content with sharp spectral peaks. Several of the non-excitation peaks align with features in the unforced baseline spectrum shown in figure 8. These results indicate that broadband forcing organises the intrinsic dynamics around pre-existing receptive bands rather than adding a flat background. Overall, the multi-frequency response extends the single-tone observations. Richer mixtures transmit more high-frequency content via larger f_c and

https://doi.org/10.1017/jfm.2026.11892 Published online by Cambridge University Press

ϕ	Excitation [Hz]	Δf [Hz]	δ_A [%]	δ_E [%]	$\Delta\phi_{tot}$ / $\Delta\phi_{cyc}$ [deg.]
0.4	220	0.741	0.068	0.135	−7.30 / −1.21
	437	0.550	0.038	0.075	−5.44/ −0.45
	800	0.652	0.058	0.115	+6.74 / +0.29
0.5	220	0.822	0.058	0.115	−6.75 / −1.34
	437	0.840	0.074	0.148	−7.63/ −0.69
	800	0.203	0.005	0.009	+1.91 / +0.09
0.6	220	0.909	0.071	0.142	−7.47 / −1.49
	437	0.492	0.025	0.051	−4.46 / −0.41
	800	0.963	0.095	0.191	−8.67 / −0.43
0.7	220	0.944	0.076	0.153	−7.76 / −1.55
	437	0.492	0.025	0.051	−4.46 / −0.41
	800	0.963	0.095	0.191	−8.67 / −0.43

Table 2. The DMD detuning metrics at each equivalence ratio ϕ and excitation frequency. Columns list the frequency offset Δf, the amplitude and energy errors δ_A and δ_E and the phase drift over the analysis window and per cycle ($\Delta\phi_{tot}$, $\Delta\phi_{cyc}$). Definitions are given in the text.

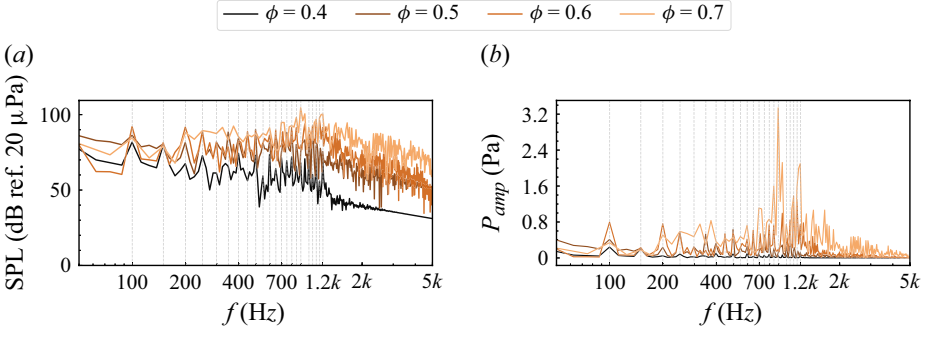


Figure 10. The SPL spectra for $\phi = 0.4.0.5, 0.6, 0.7$ flames under multi-frequency excitation: (a) shows the spectral response to an excitation signal composed of frequencies from 100 to 1200 Hz at 50 Hz intervals, and (b) shows the corresponding pressure amplitudes. Vertical dashed lines indicate the excitation frequencies. SPL (dB ref. 20 μPa) is plotted against frequency (Hz) on a logarithmic scale.

weak nonlinearity redistributes energy selectively toward baseline-preferred bands. While the SPL spectra reveal which frequencies are amplified, they do not identify the underlying thermoacoustic coupling mechanism. The modal Rayleigh framework developed in § 3 now provides this mode-resolved causality.

4.6. *Spectral analysis of the flame response*

4.6.1. *Detuning and reconstruction accuracy*

Before the modal RI $R_k(f)$ and the quadrature spectrum are analysed, the DMD identification accuracy of the forcing–locked mode at the excitation frequency is quantified. Table 2 summarises detuning and reconstruction metrics across all cases.

For a true harmonic temporal coefficient $a(t) = \mathrm{e}^{i\omega_0 t}$ and its DMD estimate $\hat{a}(t) = \mathrm{e}^{i(\omega_0+\varepsilon)t}$ over a window of duration T, the normalised projection is

$$\rho = \left| \frac{1}{T} \int_0^T \mathrm{e}^{i\varepsilon t}\, \mathrm{d}t \right| = \left| \mathrm{sinc}\left(\frac{\varepsilon T}{2}\right) \right|, \quad \varepsilon = 2\pi\, \Delta f, \quad \mathrm{sinc}\, x \equiv \frac{\sin x}{x}. \tag{4.2}$$

https://doi.org/10.1017/jfm.2026.11892 Published online by Cambridge University Press

Based on this projection, the detuning metrics are defined as

$$\delta_A \equiv 100\,(1-\rho)\ \%, \quad \delta_E \equiv 100\left(1-\rho^2\right)\%, \quad \Delta\phi_{tot} \equiv \varepsilon T\,\frac{180^\circ}{\pi}, \quad \Delta\phi_{cyc} \equiv \frac{\Delta f}{f_{exc}}\,360^\circ, \tag{4.3}$$

with f_{exc} the excitation frequency. Across all cases, $\Delta f < 1$ Hz, yielding $\delta_A < 0.1\ \%$ and $\delta_E < 0.2\ \%$. The total phase drift satisfies $|\Delta\phi_{tot}| \leq 9^\circ$ (i.e. $|\Delta\phi_{cyc}| < 1.5^\circ$ at the lowest f_{exc}). These bounds indicate that the imposed forcing is captured with high fidelity; thus the features in $R_k(f)$, $Q^{\perp}(f)$ and $Q^{eff}(f)$ discussed below may be interpreted as physical rather than as artefacts of detuning.

Free variation of the DMD window length for the forced cases is not applicable without violating the grid-alignment condition and artificially inflating cross-modal leakage. Therefore, the convergence of R_k is assessed analytically. As a further numerical check, table 1 in the supplementary material reports, for each case, the median/95th/maximum of the dimensionless product $|\sigma|T$ together with the corresponding kernel deviations $F(\sigma, T) - 1 = \mathrm{e}^{2\sigma T} - 1/2\sigma T - 1$. When $|\sigma|T \ll 1$, the DMD mode is near neutral growth (limit-cycle-like): its amplitude changes only by a factor $\mathrm{e}^{\sigma T} \approx 1 + \sigma T$ over the analysis window, so $F(\sigma, T) \approx 1$ and the modal Rayleigh quantities can be evaluated with the neutral-growth approximation. All reported values are vanishingly small; therefore we adopt $F(\sigma, T) \approx 1$ in what follows. The robustness of the dominant mode shapes to window length and start position is additionally verified directly on the unforced flames, where no grid-alignment constraint applies, by comparing the spatial modes across window configurations. More details about the sensitivity analysis can be found in the supplementary material.

For completeness, the framework remains valid when transiently growing/decaying modes are present ($|\sigma|T \not\ll 1$): in that case one should retain the exact kernel $F(\sigma, T)$ and include the finite-window cross-terms $J_{k\ell}(T)$ $(k \neq \ell)$ in the spectral sums to avoid bias from growth/decay and modal leakage.

4.6.2. *Trends in R_k, $Q^{\perp}$ and Q^{eff}*

The flame is subjected to single-frequency forcing and the measurements are performed in an anechoic environment. As a consequence, the only imposed pressure component is the excitation frequency itself. Any additional spectral content arises from the flame dynamics. This means that coupling at frequencies other than the drive frequency originates from the flame acting as a distributed acoustic source, where heat-release fluctuations at one location excite pressure fluctuations generated elsewhere in the flame.

With increasing equivalence ratio ϕ, the spectral shape of the modal RI R_k evolves systematically, as shown in figure 11. At $f_{exc} = 800$ Hz the R_k peak narrows from lean to rich conditions (smaller full width at half-maximum, indicating increased modal selectivity (higher effective Q), and its prominence within each panel becomes clearer around $\phi \approx 0.6$. At the lower forcing frequencies (220 and 437 Hz), enrichment strengthens the relative weight of harmonics: secondary maxima at integer multiples of the drive become more visible compared with the fundamental within each panel. These trends, i.e. peak narrowing (smaller half-maximum width) and increasing harmonic-to-fundamental content, are consistent with stronger nonlinear coupling and spectral redistribution beyond the imposed frequency. Note that each spectrum is normalised independently, so inter-panel amplitudes are not directly comparable. Statements here refer to shape, bandwidth and harmonic ratios that are invariant to the panel scaling. For completeness, it is also

https://doi.org/10.1017/jfm.2026.11892 Published online by Cambridge University Press

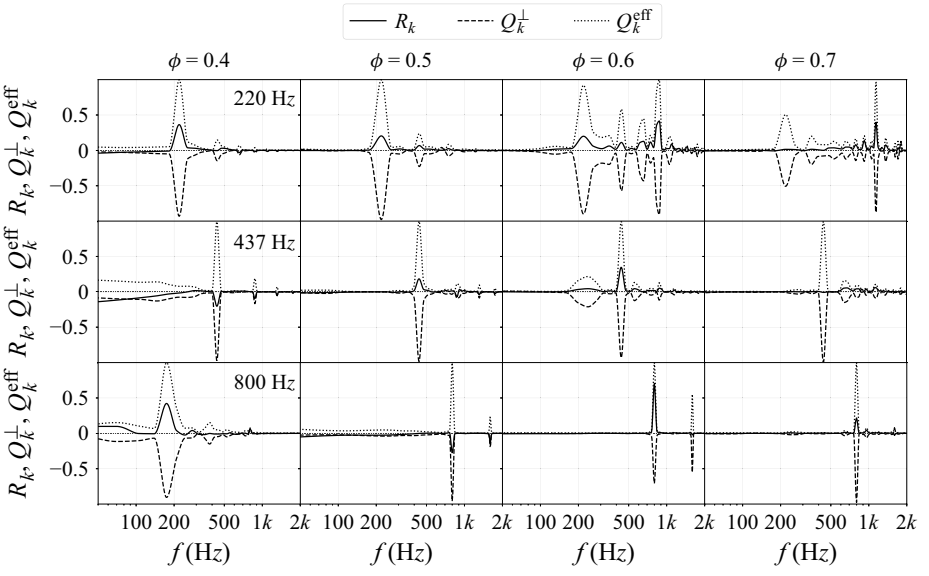


Figure 11. Frequency spectra of the modal RI R (in-phase coupling), the raw quadrature $Q^{\perp}$ (90° phase-shifted coupling) and the phase-invariant efficiency Q^{eff} for single-tone forcing at 220, 437 and 800 Hz (rows) and equivalence ratios $\phi = 0.4$, 0.5, 0.6, 0.7 (columns). Each panel is normalised independently (per-case scaling); amplitudes are comparable within a panel.

noted that the absolute coupling (e.g. the unscaled peak $|R_k(f_{exc})|$ or integrated in-phase power) typically increases with ϕ because global HRR fluctuations grow with enrichment.

Across all cases, the phase-invariant efficiency Q_k^{eff} exhibits larger and sharper peaks, being enriched at the fundamental and selected harmonics, although its spectral maxima need not coincide with those of R_k. The quantities R_k and Q_k^{eff} co-peak notably at 800 Hz at the fundamental frequency and, for 220 Hz forcing near its fourth harmonic frequency at ~ 0.88 kHz. The corresponding mode is simultaneously prominent in in-phase drive and in quadrature efficiency. At other harmonics, Q_k^{eff} may be large while R_k remains low, indicating strong quadrature coupling without significant in-phase feedback at that frequency. Maps of the local quadrature density $\mathrm{Im}\{\hat{p}_k \hat{q}_k^*\}$ highlight regions with quarter-cycle phase offsets which are most prominently observed near the flame tip. This is consistent with transport-induced phasing that intensifies with enrichment.

A comparison across forcing frequencies evidences further distinctions. At 220 Hz, the enriched flame excites a cascade of harmonics with R_k and Q_k^{eff} features extending to at least $3f$. At 437 Hz, harmonics remain visible but less pronounced and at 800 Hz, the response is dominated by the fundamental frequency with much weaker higher-order activity. Thus, low-frequency forcing promotes multi-harmonic interactions and broader spectral redistribution, whereas high-frequency forcing organises the response more selectively around a single dominant mode. With increasing ϕ, this selectivity is accompanied by a gradual shift of relative weight toward higher f that is consistent with shorter intrinsic time scales at richer conditions.

Frequencies where the modal RI is negative ($R_k < 0$) show a marked reduction of the far-field SPL at the microphone, whereas $R_k > 0$ is associated with enhanced SPL at that frequency. This correspondence is clearest in the enriched cases. For 220 Hz forcing at $\phi = 0.6$ and 0.7, harmonic components e.g. ~ 0.66 and ~ 0.88 kHz, become comparable

https://doi.org/10.1017/jfm.2026.11892 Published online by Cambridge University Press

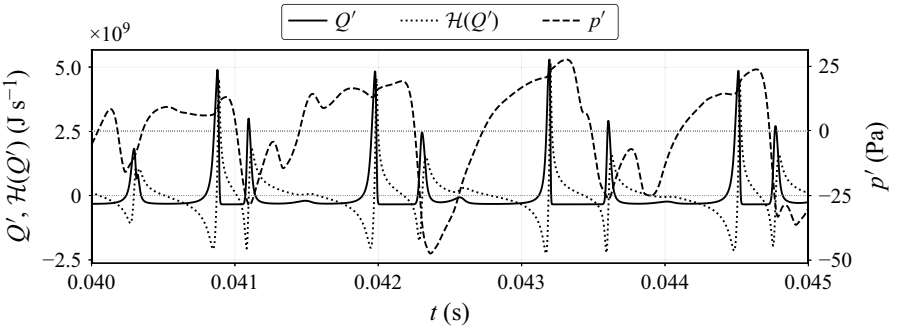


Figure 12. Local time traces of unsteady heat-release rate Q', its Hilbert transform $\mathcal{H}(Q')$ (a 90° phase shift) and the total pressure fluctuation p' at the flame tip of the $\phi = 0.7$, $f_{exc} = 800$ Hz case.

to or louder than the 220 Hz fundamental frequency in the SPL, mirroring the large Q_k^{eff} and finite R_k observed at those harmonics.

4.6.3. *Local mechanism of negative quadrature at the tip*

To relate the modal spectral behaviour to the underlying flame response, we examine the local unsteady heat-release and pressure signals at the flame tip, where the modal analysis indicates the strongest negative quadrature. Figure 12 shows that the heat-release rate exhibits sharp bursts superimposed on an approximately sinusoidal pressure signal. These bursts occur slightly before of the nearby pressure extrema such that the effective phasor product satisfies $\mathrm{Im}\{p\,\hat{q}^*\} < 0$. In a compact-source approximation, a source exactly in phase with a pressure maximum would produce no quadrature, whereas an advance of the heat release relative to the pressure leads to a negative value. This behaviour is consistent with the wrinkle–convection dynamics at the flame tip and supports the interpretation of the modal quadrature as a physically meaningful phase relation between p and $\dot{q}'$, while its magnitude indicates the strength of the coupling between pressure field and heat-release fields.

This interpretation was further examined by computing the broadband quadrature

$$Q_{bb} = \frac{1}{T}\int_{t_0}^{t_0+T} p'(t)\,\mathcal{H}\{\dot{q}'(t)\}\,\mathrm{d}t, \tag{4.4}$$

where $\mathcal{H}\{\cdot\}$ denotes the Hilbert 90° phase shift and primes indicate zero-mean fluctuations. For the temporal window shown in figure 12, the broadband quadrature Q_{bb} is negative, indicating that the local heat release tends to lead the acoustic pressure in phase. This phase advance accounts for the negative values observed in the quadrature spectra and provides a direct time-domain confirmation of the frequency-domain analysis.

4.6.4. *Cumulative RI*

After having assessed the origin of the negative quadrature through local time-domain analysis, we next examine how the net thermoacoustic energy exchange is distributed along the flame using the cumulative RI. Figure 13 shows the normalised cumulative RI along the normalised flame height. This enables a direct comparison of the three excitation frequencies for each equivalence ratio. In all cases, the coupling is tip dominated, with the largest positive contributions for $y/L \gtrsim 0.7$. The dominant coupling frequency systematically shifts with enrichment: at $\phi = 0.4$, the 220 Hz mode shows the strongest cumulative RI; at $\phi = 0.5$–0.6, 437 Hz becomes dominant, surpassing the

https://doi.org/10.1017/jfm.2026.11892 Published online by Cambridge University Press

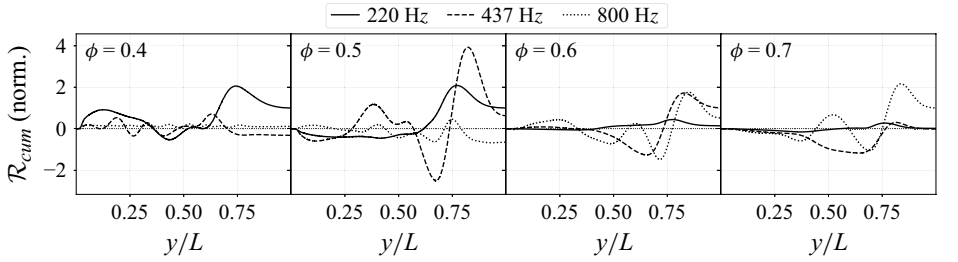


Figure 13. Cumulative RI versus normalised flame height (y/L) for equivalence ratios $\phi = 0.4$, 0.5, 0.6, 0.7. Lines show 220 (solid), 437 (dashed) and 800 Hz (dotted) excitation frequencies. Within each equivalence ratio case, all frequencies are normalised by the maximum absolute RI value across the three frequencies, preserving relative magnitudes. Positive values indicate thermoacoustic excitation, negative values indicate thermoacoustic absorption.

220 Hz contribution; at $\phi = 0.7$, energy redistributes toward 800 Hz, which now exhibits the strongest coupling, while the 220 Hz contribution diminishes. This trend is consistent with increased flame reactivity at higher ϕ, i.e. shorter intrinsic time scales, enabling the flame to couple more effectively with higher-frequency acoustic modes. This behaviour aligns with observations that hydrogen enrichment produces more compact flames with higher gain cutoff frequencies (Æsøy *et al.* 2020; Lim *et al.* 2021), making them responsive to a broader range of acoustic perturbations (Aguilar *et al.* 2022). This shifts the effective response toward higher excitation frequencies. Local negative excursions mid-flame mark antiphase interaction that partly compensates the tip excitation. Overall, the figure indicates tip-dominated coupling with a systematic frequency shift toward higher f with increasing ϕ.

Figure 13 also indicates that at higher equivalence ratios a strong cumulative RI at the excitation frequency is mainly observed when the flame remains directly coupled to the excitation. When the response redistributes energy into harmonics, the RI at the fundamental frequency tends to decrease. This outcome is consistent with the definition of the RI. The modal contribution at f_{exc} scales with the in-phase cross-spectrum $Re\{P(f_{exc})Q^*(f_{exc})\}$. As waveform distortion increases, the heat-release spectrum spreads from f_{exc} to $2f_{exc}, 3f_{exc}, \ldots$ (figure 5), which reduces $Q(f_{exc})$ and lowers phase coherence with $P(f_{exc})$. Spatial phase variations can also lead to mid-flame negative contributions that partly offset the tip excitation in the cumulative integral. By contrast, when the flame stays phase locked at f_{exc}, especially at 800 Hz for richer mixtures, the fundamental frequency remains dominant and the cumulative RI increases, yielding the tip-dominated profiles in figure 13.

4.7. *Spectral analysis of multi-frequency response*

Figure 14 presents the frequency-resolved modal RI and quadrature metrics for simulations with multi-frequency forcing, for which the excitation comprises tones at multiples of $f_0 = 50$ Hz within the range from 100 to 1200 Hz. Across equivalence ratios, enrichment shifts the band of effective thermoacoustic feedback toward higher frequencies while increasing spectral selectivity. Lean flames exhibit poor or weak responses at the upper end of the frequency range, whereas richer flames sustain narrow, positive peaks at higher mf_0. This behaviour reflects the shorter chemical time scales associated with enrichment and consequently the enhanced capacity of the flames to maintain high-frequency coupling. Because the configuration is anechoic, these trends are governed by the flame's intrinsic hydrodynamic/TD global modes: the response selectively amplifies frequencies that are

https://doi.org/10.1017/jfm.2026.11892 Published online by Cambridge University Press

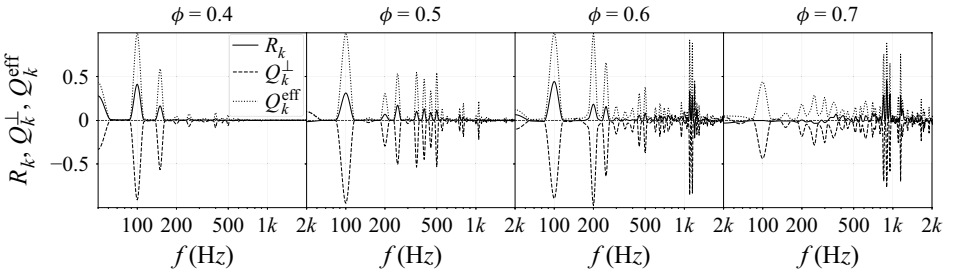


Figure 14. Frequency spectra of the modal RI R (in-phase coupling), the raw quadrature $Q^{\perp}$ (90° phase-shifted coupling) and the phase-invariant efficiency Q^{eff} for multi-frequency forcing at equivalence ratios $\phi = 0.4, 0.5, 0.6, 0.7$ (columns). Each panel is normalised independently (per-case scaling); amplitudes are comparable within a panel.

least stable in the unforced spectrum and exhibits phase-coherent growth for frequencies within the entrainment windows around those natural bands. For the richer mixtures these bands extend to approximately 1 kHz, well above the advection cutoff $f_c = 1/\tau \approx 270$ Hz for $\phi = 0.7$, so the high-frequency coupling must originate from the intrinsic cellular dynamics rather than from inlet-forced convective transport. This is corroborated by the acoustic emission of the same unforced configuration (Pedro-Beltran *et al.* 2026), which shows a prominent SPL peak between 1050 and 1200 Hz for $\phi = 0.6$ at zero external excitation. The lean $\phi = 0.4$ flame, lacking intrinsic modes in this range, serves as a natural control, its index decaying toward the upper frequencies in line with the low-pass picture.

Since the excitation resides on a harmonic grid, harmonics and intermodulation products frequently coincide with the imposed frequencies. Nonlinear redistribution therefore manifests as reweighting of the line spectrum on the 50 Hz grid rather than through frequency shifts alone. Specifically, low-frequency contributions diminish at increasing ϕ. At $\phi = 0.7$, the low-frequency modal RI becomes negligible, while higher excitation frequencies dominate in magnitude and phase coherence. This progression intensifies with enrichment and aligns with the far-field spectra observed under multi-tone forcing.

The feedback relevance inferred from figure 14 corroborates the acoustic measurements. Frequencies exhibiting positive modal Rayleigh indices correspond to elevated far-field SPL in the multi-frequency cases, while negative values align with reduced far-field levels. This correspondence confirms that the modal Rayleigh framework successfully isolates the spectral content exciting thermoacoustic instability under simultaneous multi-tone excitation.

5. Conclusions

A modal Rayleigh framework is introduced that embeds the classical Rayleigh criterion directly within the DMD of reacting flows. The formulation yields mode-specific measures of thermoacoustic excitation and absorption that are frequency resolved and expressed in closed form. By construction, the approach links temporal growth rates and oscillation frequencies to the spatial distribution of thermoacoustic coupling, enabling a direct assessment of which modes most actively satisfy or violate the Rayleigh criterion.

The methodology was applied to acoustically forced hydrogen–air slit flames over a range of equivalence ratios and forcing frequencies. The analysis of cycle-resolved flame fields, integrated response metrics and cumulative Rayleigh indices highlighted clear differences between lean and rich mixtures. Lean flames tended to follow the external

https://doi.org/10.1017/jfm.2026.11892 Published online by Cambridge University Press

excitation approximately linearly at low to intermediate frequencies, but decoupled at higher frequencies when the forcing time scale became shorter than the chemical response time. Richer mixtures remained locked into high-frequency forcing, yet exhibited stronger nonlinear distortion at lower frequencies, with secondary harmonics altering the effective coupling. In all cases the RI was found to be tip dominated, with spatial regions of antiphase response partially compensating the positive excitation near the tip.

Beyond these trends, the modal Rayleigh analysis yields three important insights that highlight its unique advantages over classical approaches: (i) it provides mode-resolved causality at single-tone and multi-tone forcing, with positive modal Rayleigh indices indicating net excitation of the acoustic field and negative values indicating an absence of net thermoacoustic driving that corresponds to a local energy sink rather than a true source of damping; (ii) by separating a phase-invariant coupling magnitude from the in-phase contribution, it distinguishes coupling strength from phase alignment and identifies bands that are strongly coupled yet thermoacoustically ineffective without phase coherence; and (iii) it localises where the coupling occurs and tracks how this spatial distribution, together with the associated positive-coupling bands, shifts with equivalence ratio toward higher frequencies with enrichment.

6. Outlook

The present analysis focused on single-frequency and multi-tone frequency forcing of canonical hydrogen–air slit flames, using the modal Rayleigh framework to characterise how equivalence ratio and forcing frequency shape the thermoacoustic response. Next, the framework will be coupled with APE analyses. By projecting DMD fields onto the APE source paths (heat release, entropy, etc.) and evaluating their interaction with the APE-predicted acoustic field, the framework can be extended to source-resolved, mode-wise rankings. This separates pseudo-sound from acoustics and clarifies the relative importance of distinct acoustic pathways. Beyond canonical configurations, the same approach could be applied to high-pressure flames, multi-injector geometries and turbulent reacting flows, where mode interactions are more complex. More generally, embedding additional physical operators within the DMD workflow enables mode-resolved diagnostics of instability excitations, resulting in a systematic route toward fully mode-aware thermoacoustic stability analysis.

Supplementary material and movies. Supplementary material and movies are available at https://doi.org/10.1017/jfm.2026.11892.

Acknowledgements. The authors gratefully acknowledge the computational resources provided by CSC – IT Centre for Science (Finland) and the Gauss Centre for Supercomputing e.V., which enabled access to the Mahti supercomputer and the GCS system HAWK at the High-Performance Computing Centre Stuttgart (HLRS), making the large-scale simulations in this study possible.

Funding. This work was supported by the Deutsche Forschungsgemeinschaft (DFG, German Research Foundation) under grant number SCHR 309/81-1 and grant number IRTG 2983 (HyPotential: Hydrogen – Fundamentals of Production, Storage & Transport, Applications, and Economy).

Declaration of interests. The authors report no conflict of interest.

References

Æsøy, E., Aguilar, J.G., Wiseman, S., Bothien, M.R., Worth, N.A. & Dawson, J.R. 2020 Scaling and prediction of transfer functions in lean premixed H_2/CH_4-flames. *Combust. Flame* **215**, 269–282.

Aguilar, J.G., Æsøy, E. & Dawson, J.R. 2022 The influence of hydrogen on the stability of a perfectly premixed combustor. *Combust. Flame* **245**, 112323.

https://doi.org/10.1017/jfm.2026.11892 Published online by Cambridge University Press

ALBAYRAK, A., ULHAQ, A., BLUMENTHAL, R.S. & POLIFKE, W. 2014 Analytical derivation of laminar premixed flame impulse response to equivalence ratio perturbations. In *Proceedings of the 21st International Congress on Sound and Vibration*, pp. 13–17. International Institute of Acoustics and Vibration (IIAV).

BECHTOLD, J.K. & MATALON, M. 2001 The dependence of the Markstein length on stoichiometry. *Combust. Flame* **127** (1), 1906–1913.

BEER, J.M. 2000 Combustion technology developments in power generation in response to environmental challenges. *Prog. Energy Combust. Sci.* **26** (4–6), 301–327.

BEERER, D., MCDONELL, V., THERKELSEN, P. & CHENG, R.K. 2014 Flashback and turbulent flame speed measurements in hydrogen/methane flames stabilized by a low-swirl injector at elevated pressures and temperatures. *J. Engng Gas Turbines Power* **136** (3), 031502.

BELTRAN, B.P., HERFF, S., PAUSCH, K., MEINKE, M. & SCHRÖDER, W. 2022 Analysis of the impact of chemistry models on the non-equidiffusion effects of lean premixed hydrogen flames. In *AIAA Scitech Forum*. American Institute of Aeronautics and Astronautics (AIAA).

BERGER, L., KLEINHEINZ, K., ATTILI, A. & PITSCH, H. 2019 Characteristic patterns of thermodiffusively unstable premixed lean hydrogen flames. *Proc. Combust. Inst.* **37**, 1879–1886.

BOUSHAKI, T., DHUÉ, Y., SELLE, L., FERRET, B. & POINSOT, T. 2012 Effects of hydrogen and steam addition on laminar burning velocity of methane–air premixed flame: experimental and numerical analysis. *Intl J. Hydrogen Energy* **37** (11), 9412–9422.

CANDEL, S. 2002 Combustion dynamics and control: progress and challenges. *Proc. Combust. Inst.* **29** (1), 1–28.

CHU, B.T. 1965 On the energy transfer to small disturbances in fluid flow (part I). *Acta Mechanica* **1** (3), 215–234.

CORREA, S.M. 1993 A review of NO_x formation under gas-turbine combustion conditions. *Combust. Sci. Technol.* **87**, 329–362.

DUPUY, A., DOUASBIN, Q. & POINSOT, T. 2024 Control of intrinsic thermoacoustic instabilities for methane and hydrogen air flames: DNS and network analysis. *Proc. Combust. Inst.* **40** (1–4), 105217.

DUROX, D., SCHULLER, T., NOIRAY, N., BIRBAUD, A.-L. & CANDEL, S. 2009 Rayleigh criterion and acoustic energy balance in unconfined self-sustained oscillating flames. *Combust. Flame* **156** (1), 106–119.

DUWIG, C. & IUDICIANI, P. 2010 Extended proper orthogonal decomposition for analysis of unsteady flames. *Flow Turbul. Combust.* **84** (1), 25–47.

FAHY, F. & GARDONIO, P. 2003 *Sound Intensity*, 2nd edn. CRC Press.

FERRAROTTI, M., DE PAEPE, W. & PARENTE, A. 2021 Reactive structures and NOx emissions of methane/hydrogen mixtures in flameless combustion. *Intl J. Hydrogen Energy* **46** (68), 34018–34045.

FFOWCS WILLIAMS, J.E. 1969 Hydrodynamic noise. *Annu. Rev. Fluid Mech.* **1**, 197–222.

GARCIA, A.M., LE BRAS, S., PRAGER, J., BOXX, I. & POLIFKE, W. 2024 Impact of H_2-enrichment on the response of a partially premixed CH_4–air flame to velocity and equivalence ratio fluctuations. *Combust. Flame* **268**, 113595.

GEISER, G., NAWROTH, H., HOSSEINZADEH, A., ZHANG, F., BOCKHORN, H., HABISREUTHER, P., JANICKA, J., PASCHEREIT, C.O. & SCHROEDER, W. 2014 Thermoacoustics of a turbulent premixed flame. In *20th AIAA/CEAS Aeroacoustics Conference*, p. 2476. American Institute of Aeronautics and Astronautics (AIAA).

GEORGE, K.J. & SUJITH, R.I. 2011 On Chu′s disturbance energy. *J. Sound Vib.* **330** (22), 5280–5291.

GEORGE, K.J. & SUJITH, R.I. 2012 Disturbance energy norms: a critical analysis. *J. Sound Vib.* **331** (7), 1552–1566.

GHANI, A., GAO, Y., DUWIG, C. & STEINBERG, A.M. 2015 Large eddy simulation of longitudinal and transverse self-excited combustion instabilities in a bluff-body stabilized turbulent premixed flame. *Combust. Flame* **162** (11), 4241–4257.

HAIDER, A., MOREV, I., RINTANEN, A., SHAHIN, Z., TAMADONFAR, P., KARIMKASHI, S., WEHRFRITZ, A. & VUORINEN, V. 2025 Accelerated numerical simulations of hydrogen flames: open-source implementation of an advanced diffusion model library in OpenFOAM. *Intl J. Hydrogen Energy* **189**, 152115.

HERFF, S., PAUSCH, K., NAWROTH, H., SCHLIMPERT, S., PASCHEREIT, C.O. & SCHRÖDER, W. 2020 Impact of burner plenum acoustics on the sound emission of a turbulent lean premixed open flame. *Intl J. Spray Combust. Dyn.* **12**, 1756827720956906.

HINDMARSH, A.C., BROWN, P.N., GRANT, K.E., LEE, S.L., SERBAN, R., SHUMAKER, D.E. & WOODWARD, C.S. 2005 SUNDIALS: Suite of nonlinear and differential/algebraic equation solvers. *ACM Trans. Math. Softw. (TOMS)* **31** (3), 363–396.

https://doi.org/10.1017/jfm.2026.11892 Published online by Cambridge University Press

HUANG, C., ANDERSON, W.E., HARVAZINSKI, M.E. & SANKARAN, V. 2016 Analysis of self-excited combustion instabilities using decomposition techniques. *AIAA J.* **54** (9), 2791–2807.
IHME, M. & PITSCH, H. 2012 On the generation of direct combustion noise in turbulent non-premixed flames. *Intl J. Aeroacoust.* **11** (1), 25–78.
Institute of Aerodynamics (AIA) 2024 m-AIA (multi-physics AIA) (v2024.1). Zenodo. Available at: https://doi.org/10.5281/zenodo.13350586.
KANG, H. & KIM, K.T. 2021 Combustion dynamics of multi-element lean-premixed hydrogen-air flame ensemble. *Combust. Flame* **233**, 111585.
KANG, H., LEE, M. & KIM, K.T. 2023 Measurements of self-excited instabilities and nitrogen oxides emissions in a multi-element lean-premixed hydrogen/methane/air flame ensemble. *Proc. Combust. Inst.* **39** (4), 4721–4729.
KARIMI, N. 2014 Response of a conical, laminar premixed flame to low amplitude acoustic forcing–a comparison between experiment and kinematic theories. *Energy* **78**, 490–500.
KEE, R.J., COLTRIN, M.E., GLARBORG, P. & ZU, H. 2018 *Chemically Reacting Flows: Theory, Modeling, and Simulation*, 2nd edn. John Wiley and Sons, Ltd.
KOPP-VAUGHAN, K.M. & RENFRO, M.W. 2012 Flame shape and spatially resolved Rayleigh criterion using proper orthogonal decomposition. *Intl J. Spray Combust. Dyn.* **4** (3), 255–274.
LEE, J.G. & SANTAVICCA, D.A. 2003 Experimental diagnostics for the study of combustion instabilities in lean premixed combustors. *J. Propul. Power* **19** (5), 735–750.
LEE, T. & KIM, K.T. 2020 Combustion dynamics of lean fully-premixed hydrogen-air flames in a mesoscale multinozzle array. *Combust. Flame* **218**, 234–246.
LEFEBVRE, A.H. & BALLAL, D.R. 2010 *Gas Turbine Combustion: Alternative Fuels and Emissions*. CRC press.
LI, J., ZHAO, Z., KAZAKOV, A. & DRYER, F.L. 2004 An updated comprehensive kinetic model of hydrogen combustion. *Intl J. Chem. Kinet.* **36** (10), 566–575.
LIEUWEN, T. 2003 Modeling premixed combustion-acoustic wave interactions: a review. *J. Propul. Power* **19** (5), 765–781.
LIEUWEN, T.C. 2021 *Unsteady Combustor Physics*. Cambridge University Press.
LIM, Z., LI, J. & MORGANS, A.S. 2021 The effect of hydrogen enrichment on the forced response of CH4/H2/Air laminar flames. *Intl J. Hydrogen Energy* **46** (46), 23943–23953.
LIOU, M.-S. & STEFFEN, C.J. 1993 A new flux splitting scheme. *J. Comput. Phys.* **107** (1), 23–39.
LODATO, G., DOMINGO, P. & VERVISCH, L. 2008 Three-dimensional boundary conditions for direct and large-eddy simulation of compressible viscous flows. *J. Comput. Phys.* **227** (10), 5105–5143.
LU, T. & LAW, C.K. 2009 Toward accommodating realistic fuel chemistry in large-scale computations. *Prog. Energy Combust. Sci.* **35** (2), 192–215.
MA, K., YU, X., ZHAO, X., LI, X., LI, S., ZHAO, D. & SHI, B. 2020 Response of lean premixed swirl tubular flame to acoustic perturbations. *Exp. Therm. Fluid Sci.* **119**, 110199.
MAGRI, L., JUNIPER, M.P. & MOECK, J.P. 2020 Sensitivity of the Rayleigh criterion in thermoacoustics. *J. Fluid Mech.* **882**, R1.
MCBRIDE, B.J., GORDON, S. & RENO, M.A. 1993 Coefficients for calculating thermodynamic and transport properties of individual species. *Tech. Rep.* TM-4513. NASA.
NICOUD, F. & POINSOT, T. 2005 Thermoacoustic instabilities: should the Rayleigh criterion be extended to include entropy changes? *Combust. Flame* **142** (1–2), 153–159.
NIEMEYER, K.E., CURTIS, N.J. & SUNG, C.-J. 2017 pyJac: analytical Jacobian generator for chemical kinetics. *Comput. Phys. Commun.* **215**, 188–203.
NOBLE, D., WU, D., EMERSON, B., SHEPPARD, S., LIEUWEN, T. & ANGELLO, L. 2021 Assessment of current capabilities and near-term availability of hydrogen-fired gas turbines considering a low-carbon future. *J. Engng Gas Turbines Power* **143** (4), 041002.
NOIRAY, N., DUROX, D., SCHULLER, T. & CANDEL, S. 2008 A unified framework for nonlinear combustion instability analysis based on the flame describing function. *J. Fluid Mech.* **615**, 139–167.
PARK, D., LEE, T. & KIM, K.T. 2022 Rotational symmetry-driven modal dynamics of high-frequency transverse instabilities in a lean-premixed multislit hydrogen combustor. *Combust. Flame* **245**, 112356.
PAUSCH, K., HERFF, S., NAWROTH, H., PASCHEREIT, C.O. & SCHROEDER, W. 2018 Noise sources of a lean-premixed jet flame. In *2018 AIAA/CEAS Aeroacoustics Conference*, pp. 4088. American Institute of Aeronautics and Astronautics (AIAA).
PEDRO-BELTRAN, B., SHAHIN, Z., MEINKE, M., HERFF, S., KRUG, D. & SCHRÖDER, W. 2026 Impact of thermal and differential-preferential diffusion on the dynamics and acoustics of hydrogen–air slit flames. *Combust. Flame* **286**, 114810.
PIERCE, A.D. 2019 *Acoustics: An Introduction to Its Physical Principles and Applications*, 3rd edn. Springer.

https://doi.org/10.1017/jfm.2026.11892 Published online by Cambridge University Press

POINSOT, T. 2017 Prediction and control of combustion instabilities in real engines. *Proc. Combust. Inst.* **36** (1), 1–28.

POINSOT, T. & VEYNANTE, D. 2005 *Theoretical and Numerical Combustion*. Edwards.

POINSOT, T.J. & LELE, S.K. 1992 Boundary conditions for direct simulations of compressible viscous flows. *J. Comput. Phys.* **101** (1), 104–129.

POLIFKE, W. 2020 Modeling and analysis of premixed flame dynamics by means of distributed time delays. *Prog. Energy Combust. Sci.* **79**, 100845.

PUTNAM, A.A. 1971 *Combustion-Driven Oscillations in Industry*. American Elsevier Publishing Company.

RAYLEIGH, L. 1878 The explanation of certain acoustical phenomena. *R. Inst. Proc.* **8**, 536–542.

RODRÍGUEZ-PASTOR, M., KOUMIDES, P., PÉREZ-SÁNCHEZ, E.J., GARCÍA-TÍSCAR, J., BROATCH, A. & MIRA, D. 2024 Numerical analysis of laminar velocity-forced premixed slit flames using modal decomposition techniques. *Combust. Flame* **269**, 113661.

SCHLIMPERT, S., MEINKE, M. & SCHRÖDER, W. 2016 Nonlinear analysis of an acoustically excited laminar premixed flame. *Combust. Flame* **163**, 337–357.

SCHLUP, J. & BLANQUART, G. 2018 A reduced thermal diffusion model for H and H_2. *Combust. Flame* **191**, 1–8.

SCHMID, P.J. 2010 Dynamic mode decomposition of numerical and experimental data. *J. Fluid Mech.* **656**, 5–28.

SCHUERMANS, B., MOECK, J., BLONDÉ, A., DHARMAPUTRA, B. & NOIRAY, N. 2023 The Rayleigh integral is always positive in steadily operated combustors. *Proc. Combust. Inst.* **39** (4), 4661–4669.

SCHULLER, T., DUROX, D. & CANDEL, S. 2003 A unified model for the prediction of laminar flame transfer functions: comparisons between conical and V-flame dynamics. *Combust. Flame* **134**, 21–34.

SCHULLER, T., POINSOT, T. & CANDEL, S. 2020 Dynamics and control of premixed combustion systems based on flame transfer and describing functions. *J. Fluid Mech.* **894**, P1.

TEKGÜL, B., PELTONEN, P., KAHILA, H., KAARIO, O. & VUORINEN, V. 2021 DLBFoam: an open-source dynamic load balancing model for fast reacting flow simulations in OpenFOAM. *Comput. Phys. Commun.* **267**, 108073.

VAN LEER, B. 1979 Towards the ultimate conservative difference scheme. V. A second-order sequel to Godunov's method. *J. Comput. Phys.* **32** (1), 101–136.

VANCE, F.H., ALANYALIOĞLU, Ç. & HASSE, C. 2023*a* Analysis of Lewis number effects on dynamic response of laminar premixed flames. *Combust. Flame* **248**, 112508.

VANCE, F.H., SCHOLTISSEK, A., DE GOEY, P., VAN OIJEN, J. & HASSE, C. 2023*b* Dynamic stabilization of a hydrogen premixed flame in a narrow channel. *Combust. Flame* **248**, 112560.

YANG, Y., FANG, Y., ZHONG, L., XIA, Y., JIN, T., LI, J. & WANG, G. 2021 DMD analysis for velocity fields of a laminar premixed flame with external acoustic excitation. *Exp. Therm. Fluid Sci.* **123**, 110318.

YUSAF, T., MAHAMUDE, A.S.F., KADIRGAMA, K., RAMASAMY, D., FARHANA, K., DHAHAD, H.A. & TALIB, A.B.D.R.A. 2024 Sustainable hydrogen energy in aviation A narrative review. *Intl J. Hydrogen Energy* **52**, 1026–1045.

ZHANG, F., ZIRWES, T., WANG, Y., CHEN, Z., BOCKHORN, H., TRIMIS, D. & STAPF, D. 2022 Dynamics of premixed hydrogen/air flames in unsteady flow. *Phys. Fluids* **34** (8), 085121.

ZHENG, J., LI, L., WANG, G., XIA, X., XU, L. & QI, F. 2024 Nonlinear response of conical flame to dual-frequency excitation. *Applics Energy Combust. Sci.* **18**, 100266.

https://doi.org/10.1017/jfm.2026.11892 Published online by Cambridge University Press